nature cell biology

Functional interplay between the DNA-damage-response kinase ATM and ARF tumour suppressor protein in human cancer

Georgia Velimezi[1,11], Michalis Liontos[1,11], Konstantinos Vougas[2], Theodoros Roumeliotis[2,3], Jirina Bartkova[4], Maria Sideridou[1], Ayguel Dereli-Oz[5], Maciej Kocylowski[4], Ioannis S. Pateras[1], Kostas Evangelou[1], Athanassios Kotsinas[1], Ines Orsolic[6], Sladana Bursac[6], Maja Cokaric-Brdovcak[6], Vassilis Zoumpourlis[7], Dimitris Kletsas[8], George Papafotiou[2], Apostolos Klinakis[2], Sinisa Volarevic[6], Wei Gu[9], Jiri Bartek[4,10,12], Thanos D. Halazonetis[5] and Vassilis G. Gorgoulis[1,2,12]

The DNA damage response (DDR) pathway and ARF function as barriers to cancer development. Although commonly regarded as operating independently of each other, some studies proposed that ARF is positively regulated by the DDR. Contrary to either scenario, we found that in human oncogene-transformed and cancer cells, ATM suppressed ARF protein levels and activity in a transcription-independent manner. Mechanistically, ATM activated protein phosphatase 1, which antagonized Nek2-dependent phosphorylation of nucleophosmin (NPM), thereby liberating ARF from NPM and rendering it susceptible to degradation by the ULF E3-ubiquitin ligase. In human clinical samples, loss of ATM expression correlated with increased ARF levels and in xenograft and tissue culture models, inhibition of ATM stimulated the tumour-suppressive effects of ARF. These results provide insights into the functional interplay between the DDR and ARF anti-cancer barriers, with implications for tumorigenesis and treatment of advanced tumours.

Oncogenic stimuli trigger activation of checkpoints that delay or prevent tumorigenesis. The DDR pathway and the alternative reading frame (ARF) tumour suppressor protein are two such checkpoints that act, mainly, by activating the tumour suppressor p53 (refs 1–8).

The widely held view is that the DDR and ARF pathways act independently of each other[1,9–11]. This view is largely based on murine models. Although cancer biology in both humans and mice mostly reflects the same principles, the role of ATM (ataxia telangiectasia mutated), a key DDR kinase and tumour suppressor, may be more pronounced in human cancer. Despite the well-established role of ATM in suppressing lymphoid malignancies in humans and mice[12], it was recently suggested that the tumour suppressor role of ATM in murine non-lymphoid malignancies is limited[13]. Interestingly, for a reason that is not yet clarified, *ATM*-null mouse embryo fibroblasts (MEFs) exhibit higher levels of ARF when compared with their wild-type counterparts[11]. Moreover, although the lifespan of *ATM*-null when compared with *ATM/ARF* double-null mice is similarly limited by lymphomagenesis, the latter mice develop a broader spectrum of tumours[11]. Given the intriguing open questions about ATM and ARF, and their mutual relationship in tumorigenesis, we explored the mechanistic basis of a potential interplay between ATM and ARF in human cell models and clinical settings. We discovered that ATM negatively regulates ARF abundance in a transcription-independent manner through a pathway that involves protein phosphatase-1 (PP1), Nek2 kinase and nucleophosmin (NPM/B23). We suggest that this pathway can be exploited at the clinical level particularly in advanced, p53-aberrant tumours that are very difficult to treat.

[1]Molecular Carcinogenesis Group, Department of Histology and Embryology, School of Medicine, University of Athens, 75 Mikras Asias Str, Athens, GR-11527, Greece. [2]Biomedical Research Foundation of the Academy of Athens, 4 Soranou Ephessiou St., Athens, GR-11527, Greece. [3]Centre for Proteomic Research, Institute for Life Sciences, University of Southampton, University Road, Highfield, Southampton, SO17 1BJ, UK. [4]Danish Cancer Society Research Center, Strandboulevarden 49, Copenhagen, DK-2100, Denmark. [5]Department of Molecular Biology, University of Geneva, 30 quai Ernest-Ansermet, Geneva, CH-1211, Switzerland. [6]Department of Molecular Medicine and Biotechnology, School of Medicine, University of Rijeka, Brace Branchetta 20, Rijeka, 51000, Croatia. [7]Unit of Biomedical Applications, Institute of Biology, Medical Chemistry and Biotechnology, National Hellenic Research Foundation, 48 Vassileos Constantinou Ave., Athens, GR-11635, Greece. [8]Laboratory of Cell Proliferation and Ageing, Institute of Biosciences and Applications, National Centre for Scientific Research 'Demokritos', Agia Paraskevi Attikis, PO Box 60228, Athens, GR-15310, Greece. [9]Institute for Cancer Genetics, and Department of Pathology and Cell Biology College of Physicians & Surgeons, Columbia University, 1130 St. Nicholas Ave., New York, New York 10032, USA. [10]Institute of Molecular and Translational Medicine, Faculty of Medicine and Dentistry, Palacky University, Hněvotínská 5, Olomouc, 779 00, Czech Republic. [11]These authors contributed equally to this work.
[12]Correspondence should be addressed to J. Bartek or V.G. Gorgoulis (e-mail: jb@cancer.dk or vgorg@med.uoa.gr or vgorgoulis@gmail.com)

Received 14 February 2013; accepted 24 May 2013; published online 14 July 2013; DOI: 10.1038/ncb2795

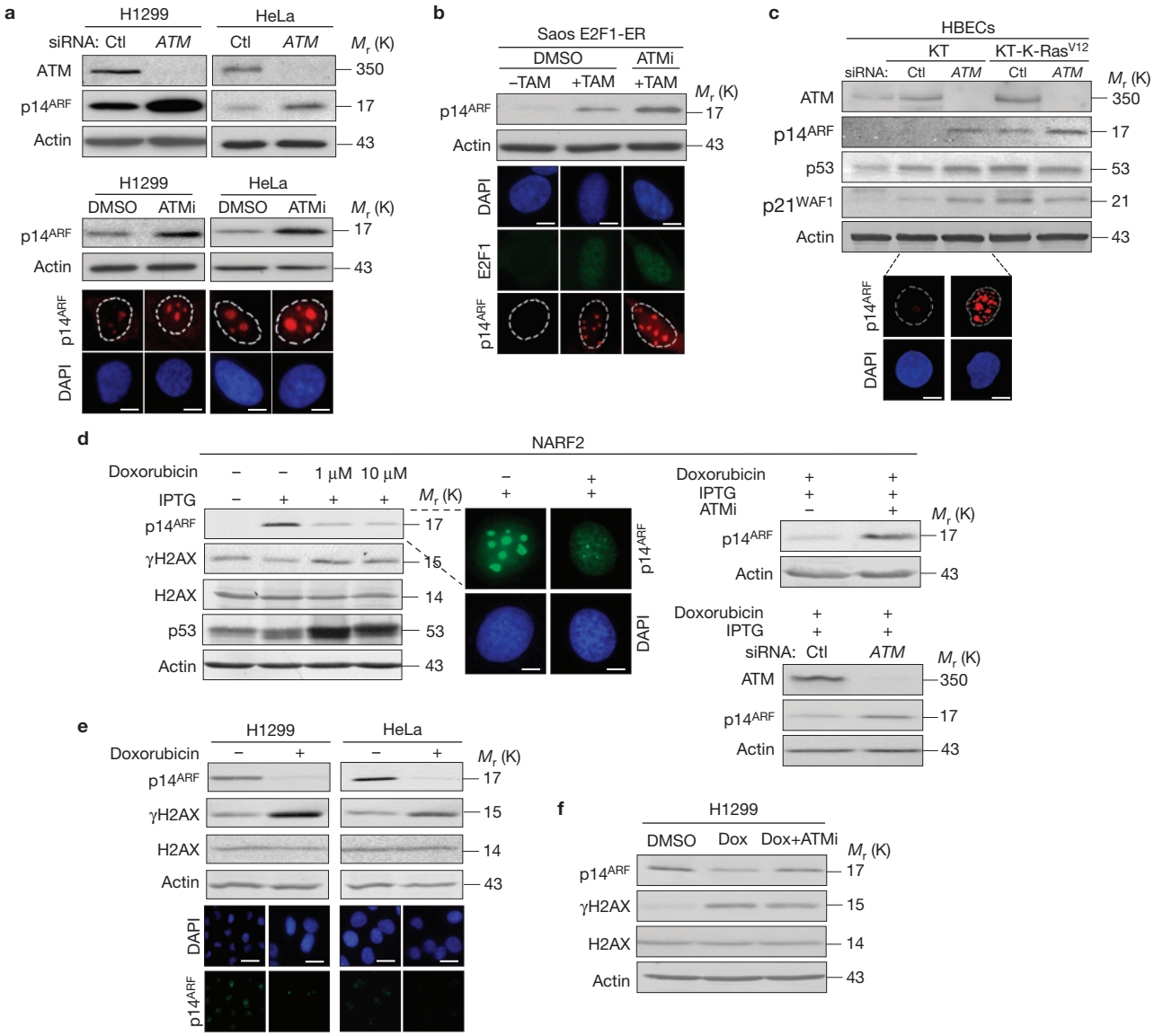

Figure 1 ATM regulates p14^{ARF} protein levels *in vitro*. (**a**) Immmunoblot demonstrating p14^{ARF} upregulation after siRNA silencing of *ATM* in H1299 and HeLa cells. Immunoblot and immunofluorescence analyses depicting that inhibition of ATM activity with Ku55933 in H1299 and HeLa cells results in p14^{ARF} upregulation, as well. Scale bars, 5 μm (HeLa) and 4 μm (H1299). (**b**) Immunoblot and immunofluorescence analyses showing an increase in p14^{ARF} protein levels after E2F1 activation (addition of 4-OH-tamoxifen) that is further enhanced by chemical inhibition of ATM (Ku55933). Scale bars, 5 μm. (**c**) Upregulation of p14^{ARF} in immortalized (KT: hTERT/Cdk4) and K-Ras^{V12}-transfected immortalized (KT) HBECs after *ATM* siRNA. Scale bars, 5 μm. (**d**) The DNA damage agent doxorubicin decreases induced p14^{ARF} protein levels in the p14^{ARF}-inducible NARF2 cell line, as shown by immunoblot and immunofluorescence analyses. Immunoblot analysis showing that chemical inhibition or genetic silencing of ATM rescues p14^{ARF} expression from the suppressive effect of doxorubicin, in NARF2 cells. Scale bars, 3 μm. (**e**) Doxorubicin treatment decreases p14^{ARF} protein levels, as assessed by immunoblot and immunofluorescence analyses, in H1299 and HeLa cells. Scale bars, 20 μm (HeLa left panel) and 10 μm (HeLa right panel and H1299). (**f**) Chemical inhibition of ATM rescues p14^{ARF} decline in doxorubicin-treated H1299 cells. Actin serves as loading control. Ctl, control siRNA; TAM, 4-OH-tamoxifen; ATMi, Ku55933; Dox, doxorubicin; IPTG, isopropyl β-D-1-thiogalactopyranoside; DMSO, dimethylsulphoxide. Uncropped images of blots are shown in Supplementary Fig. S9.

RESULTS

ARF expression is negatively regulated by ATM

To examine whether ATM regulates ARF, we first assessed ARF protein levels in human cancer cell lines after silencing ATM by short interfering RNA (siRNA) or inhibiting its activity with the Ku55933 inhibitor[14] (Supplementary Fig. S1a). Both depletion and inhibition of ATM led to increased ARF protein levels in H1299 and HeLa cells (Fig. 1a). These cells were chosen for the initial experiments because they have detectable levels of ARF protein, due to p53 inactivation[10], and the DDR pathway is constitutively activated[15] (Supplementary Fig. S1b). Interestingly, in these same cells, silencing of Chk2, the main downstream transducer kinase of ATM, had no effect on ARF levels (Supplementary Fig. S1c).

Consistently, the effect of ATM inhibition on ARF protein abundance was also observed in other cell systems, including oncogene-transformed human diploid fibroblasts and epithelial cells.

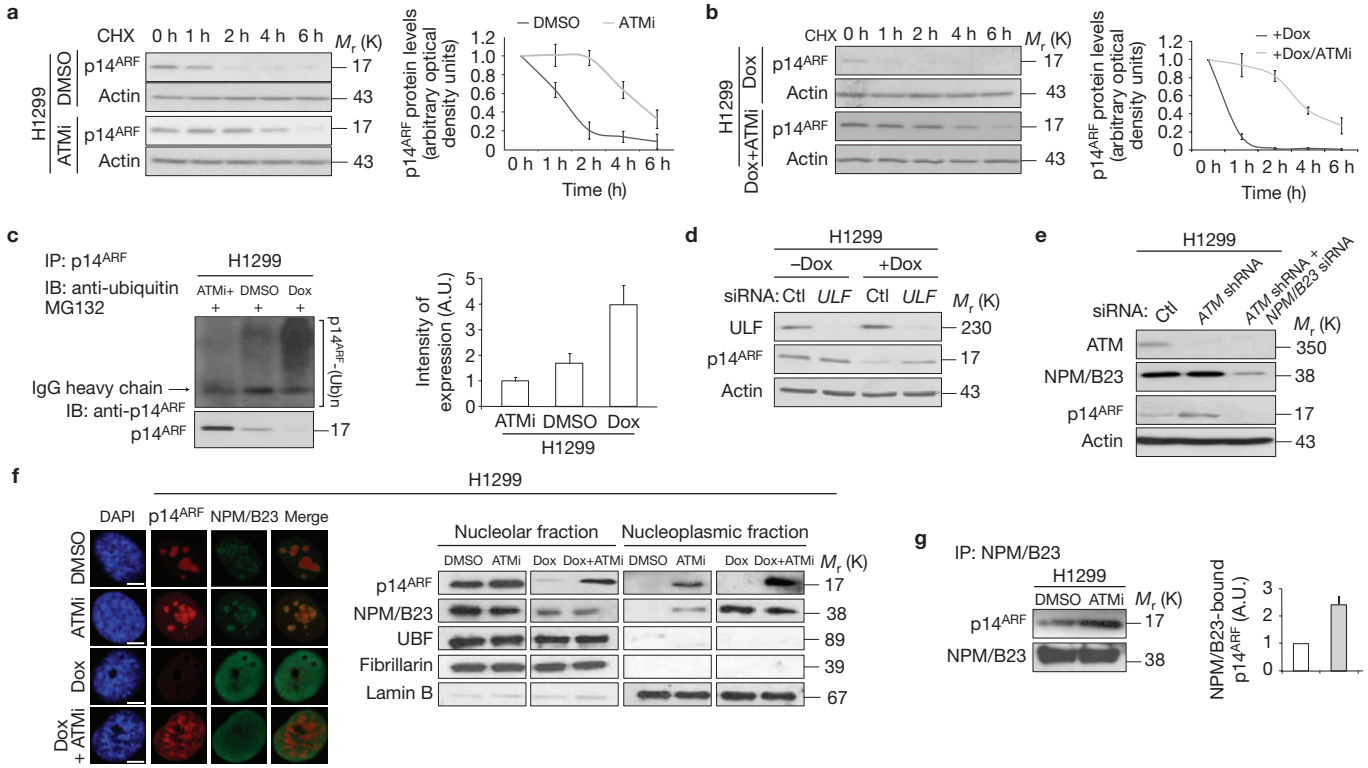

Figure 2 ATM regulates p14^{ARF} protein stability. (**a**) Immunoblot demonstrating that the mean half-life of p14^{ARF} in ATMi +CHX-treated H1299 cells is increased when compared with control (DMSO) +CHX-treated cells. Graph depicts estimated mean half-life of p14^{ARF} ($P = 0.044$, *t*-test, error bars indicate s.d., regression analysis was used to calculate p14^{ARF} half-life, $n = 5$ blots). (**b**) Immunoblot demonstrating that the mean half-life of p14^{ARF} in Dox+ATMi+CHX-treated H1299 cells is increased when compared with control (Dox)+CHX-treated cells. Graph depicts estimated mean half-life of p14^{ARF} ($P = 0.042$, *t*-test, error bars indicate s.d., regression analysis was used to calculate p14^{ARF} half-life, $n = 5$ blots). (**c**) Ubiquitylation assay revealing a gradual increase in p14^{ARF} ubiquitylation from ATMi- to DMSO- and doxorubicin-treated H1299 cells. IP, immunoprecipitation; IB, immunoblot. The histogram depicts quantification of p14^{ARF} ubiquitylation in ATMi-, DMSO- and doxorubicin-treated H1299 cells ($P = 0.001$, *t*-test, error bars indicate s.d., $n = 3$ blots). (**d**) RNAi-mediated knockdown of TRIP12/ULF rescues p14^{ARF} downregulation in doxorubicin-treated H1299 cells. (**e**) Immunoblot analysis in *ATM* shRNA treated H1299 cells shows that ATM suppression does not upregulate p14^{ARF} expression when NPM/B23 is concurrently silenced. (**f**) Immunofluorescence and nucleolar/nucleoplasmic fraction immunoblot analyses of p14^{ARF} and NPM/B23 in ATMi-, doxorubicin- and doxorubicin+ATMi-treated H1299 cells. Nuclei were counterstained with DAPI. Scale bars, 5 μm. (**g**) NPM/B23 immunoprecipitation from H1299 cells treated with DMSO or ATMi followed by immunoblotting against p14^{ARF} and total NPM/B23 shows increased binding of p14^{ARF} to NPM/B23 in ATMi-treated cells ($P < 0.001$, *t*-test, error bars indicate s.d., $n = 3$ blots). Actin serves as loading control. IPTG, isopropyl β-D-1-thiogalactopyranoside; ATMi, Ku55933; Dox, doxorubicin; CHX, cycloheximide. Uncropped images of blots are shown in Supplementary Fig. S9.

In Saos-2 cells engineered to activate the DDR pathway and upregulate ARF following E2F1 overexpression[16,17], inhibition of ATM further enhanced ARF levels (Fig. 1b and Supplementary Fig. S1d). In human bronchial epithelial cells (HBECs) expressing human telomerase (hTERT) and a Cdk4 mutant that is insensitive to p16^{INK4A} (HBEC3-KT cells) and, optionally, also oncogenic *K-Ras*^{V12} (HBEC3-KT K-Ras^{V12} cells; refs 18,19), suppression of activated ATM potentiated ARF levels (Fig. 1c and Supplementary Fig. S1f). The same effect was observed in serum-depleted[20] human diploid BJ cells transiently transfected with β-catenin (Supplementary Fig. S1g and S1h).

If inhibition of ATM enhances ARF levels, then activation of ATM should suppress ARF levels. This prediction was confirmed, as ARF protein decreased in irradiated wild-type ATM H1299 cells but not in their ATM-depleted (short hairpin RNA; shRNA) counterparts (Supplementary Fig. S1i). Moreover, U2OS cells expressing ectopic ARF in an IPTG-dependent manner[10] (NARF2 cells) were treated with IPTG and then with increasing doses of doxorubicin to activate ATM. Doxorubicin triggered an intense DDR and prevented the accumulation of IPTG-induced ARF (Fig. 1d). Importantly, the effect of doxorubicin on ARF levels was mitigated when ATM was genetically silenced or inhibited by Ku55933 (Fig. 1d). Similar effects were observed with endogenous ARF in H1299 and HeLa cells (Fig. 1e,f). These results suggest that activated ATM restrains oncogene-induced ARF expression[1] (Supplementary Fig. S1j).

ATM regulates ARF abundance in a transcription-independent manner

To explore the mechanism by which ATM regulates ARF levels, we first examined by quantitative PCR with reverse transcription (qRT–PCR) whether ATM modulates *ARF* messenger RNA levels. Although oncogene-induced ARF expression was transcription dependent (Supplementary Fig. S1d), silencing of *ATM* or inhibiting its activity had no effect on *ARF* mRNA levels (Supplementary Fig. S1e). Instead, ATM regulated ARF protein turnover, as revealed by treating H1299 cells with cycloheximide to block protein synthesis, in the presence or absence of the ATM inhibitor Ku55933, and determining ARF protein levels over time. In the cells treated with Ku55933, the half-life of ARF protein increased by 75% (Fig. 2a). Moreover, suppressing ATM

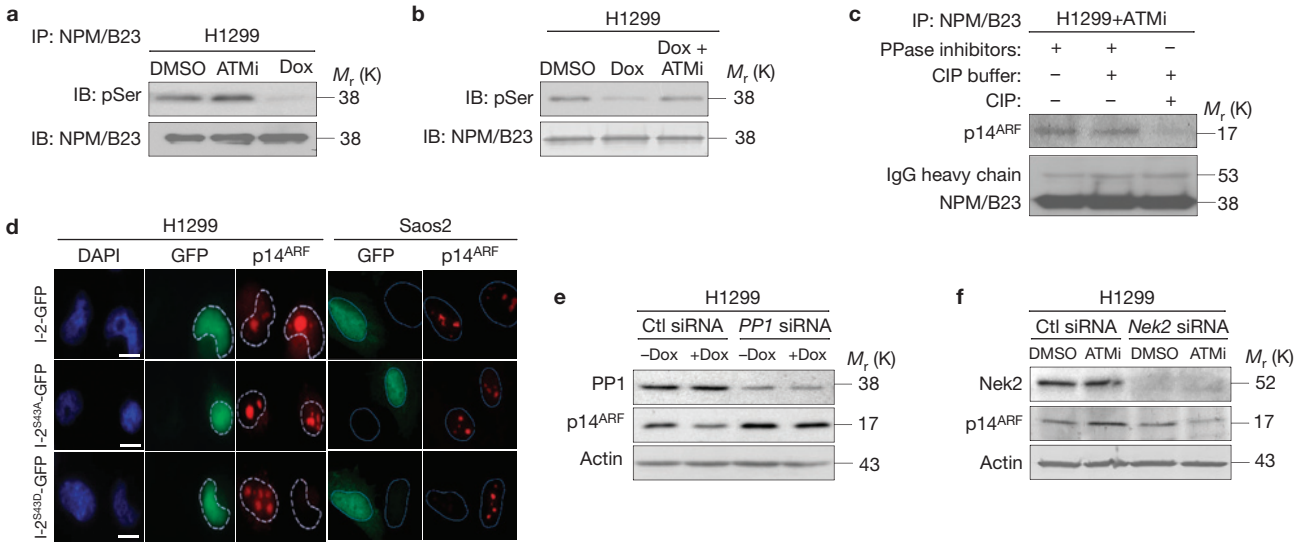

Figure 3 p14^{ARF} protein stability is regulated by the ATM–PP1–Nek2-mediated pathway. (**a**) NPM/B23 immunoprecipitation (IP) from H1299 cells treated with DMSO, ATMi and doxorubicin followed by immunoblotting (IB) against phospho-serine and total NPM/B23 show increased NPM/B23 phosphorylation in ATMi cells and decreased phosphorylation in doxorubicin-treated ones. (**b**) ATMi in doxorubicin-treated H1299 cells restores NPM/B23 phosphorylation as shown by immunoprecipitation for NPM/B23 followed by immunoblotting against phospho-serine and total NPM/B23. (**c**) NPM/B23 immunoprecipitation from H1299 cells treated with ATMi, followed by immunoblotting against p14^{ARF} and total NPM/B23 shows decreased binding of p14^{ARF} to NPM/B23 in calf intestinal phosphatase (CIP)-treated cells. (**d**) Immunofluorescence analysis demonstrating absence of p14^{ARF} staining in nuclei transfected with the phosphomimetic I-2S44D–GFP compared with I-2–GFP and the I-2S44A–GFP mutant form, in H1299 and Saos2 cells. Nuclei were counterstained with DAPI. Dotted lines define nuclei. Scale bars, 5 μm. (**e**) Silencing of PP1 prevents doxorubicin-induced downregulation of p14^{ARF} in H1299 cells, recapitulating the effect of ATMi. (**f**) Nek2 silencing inhibits upregulation of p14^{ARF} in ATMi-treated H1299 cells. Actin, lamin B, fibrillarin and RNA polymerase I transcription factor (UBF) serve as loading and/or fractionation controls. Dox, doxorubicin; ATMi, Ku55933 treatment; PPase inhibitors, phosphatase inhibitors. Uncropped images of blots are shown in Supplementary Fig. S9.

activity in doxorubicin-treated cells increased significantly the half-life of ARF demonstrating the ability of ATM inhibition to sustain ARF expression during genotoxic stress, as well (Fig. 2b). These effects of DNA damage and ATM on ARF protein half-life were mediated by ubiquitylation, as evidenced by monitoring levels of ubiquitylated ARF in H1299 cells treated with the Ku55933 inhibitor or with doxorubicin (Fig. 2c).

The ubiquitin ligase ULF is the downstream effector of the ATM-mediated ARF degradation pathway

ULF, also known as TRIP12, has been previously described as a nucleoplasmic E3 ubiquitin ligase that mediates lysine-independent ubiquitylation of ARF (ref. 21). Significantly, depletion of ULF by siRNA abrogated the effect of doxorubicin on ARF protein levels (Fig. 2d). ATM inhibition or activation did not affect ULF protein levels, suggesting that ATM could regulate the access of ARF to ULF (Supplementary Fig. S2a). It is known that ARF accumulates in the nucleolus by binding to nucleophosmin (NPM/B23), an abundant nucleolar acidic chaperone phosphoprotein that is essential for ARF stability[1,22–24], and that DNA damage results in translocation of both NPM/B23 and ARF from the nucleolus to the nucleoplasm[25,26]. Therefore, for ARF to be ubiquitylated by ULF it might need to translocate into the nucleoplasm and be released from NPM/B23 (ref. 21). Consistent with this reasoning, silencing of NPM/B23 in H1299 cells decreased ARF protein levels (Supplementary Fig. S2b). Most importantly, ARF levels remained low even when silencing of NPM/B23 was preceded by ATM suppression (Fig. 2e). This result pinpoints NPM/B23 as the downstream target of ATM that regulates the stability of ARF. Moreover, rather than preventing the translocation of NPM/B23 and ARF to the nucleoplasm (Fig. 2f), inhibition of ATM rescued ARF expression in doxorubicin-treated cells, mainly in the nucleoplasm (Fig. 2f and Supplementary Fig. S2c) and enhanced the interaction between NPM/B23 and ARF (Fig. 2g). Altogether these results suggest that activation of ATM promotes the degradation of ARF by disrupting the ARF–NPM/B23 complex.

PP1 links ATM with NPM/B23 hypophosphorylation and ARF downregulation

It has already been reported that DNA damage disrupts the ARF–NPM/B23 complex, but the underlying biochemical mechanism remained elusive[26]. The ATM dependency provided the opportunity to obtain mechanistic insights. NPM/B23 contains a large number of serines and threonines, even though typical SQ/TQ ATM phosphorylation sites are not observed[27]. To examine whether ATM-dependent phosphorylation(s) of NPM/B23 account for ARF degradation we treated H1299 cells with Ku55933 and/or doxorubicin and NPM/B23 immunoprecipitates were blotted with an antibody against phosphorylated serine residues. Surprisingly, ATM inhibition increased the fraction of phosphorylated NPM/B23, whereas doxorubicin treatment led to hypophosphorylation of NPM/B23 that was rescued when doxorubicin-exposed cells were treated with ATMi (Fig. 3a,b), implicating a potential role for an ATM-regulated phosphatase in targeting NPM/B23. Consistent with this notion, the amount of ARF bound to NPM/B23 was substantially decreased when NPM/B23

immunoprecipitation was carried out in the presence of calf intestinal phosphatase (Fig. 3c). The serine/threonine PP1 is a potential candidate because it can dephosphorylate NPM/B23 (ref. 28) and it is so far the only reported serine/threonine phosphatase activated by ATM (ref. 29). Consistently, addition of doxorubicin to H1299 cells led to a substantial increase of the phosphorylated (inactive) form of the regulatory PP1 inhibitory subunit I-2 (Supplementary Fig. S3a), thereby rendering PP1 active. To examine whether PP1 regulates ARF levels, we constructed a phosphomimetic I-2 mutant, replacing Ser 43, the residue phosphorylated by ATM, with aspartic acid[29] (S43D). Decreased phosphorylation of histone H3 at Ser 10 served as positive control of PP1 activation, in response to DNA damage, as previously reported[29] (Supplementary Fig. S3b). Strikingly, the nuclei of H1299 and Saos2 cells transfected with the phosphomimetic mutant I-2 exhibited decreased ARF expression, whereas ARF levels were unaffected in cells transfected with wild-type I-2 or I-2 bearing the dominant inhibitory Ser 43 to alanine (S43A) substitution[29] (Fig. 3d and Supplementary Fig. S3c). The phosphomimetic mutant I-2 did not affect either nucleolar integrity, as demonstrated by fibrillarin staining[30], or NPM localization, indicating that the effect is specific for ARF (Supplementary Fig. S3d,e). In addition, silencing of PP1 (all three isoforms—α, β/δ and γ; ref. 31) by siRNA led to ARF upregulation, thus mimicking ATM inhibition (Fig. 3e), further supporting a role for PP1 in ARF turnover.

Inhibition of the ATM–PP1 signalling axis activates Nek2 kinase, which phosphorylates NPM/B23 at Ser 70 and Ser 88, enhancing ARF stability

As PP1 seems to be involved in dephosphorylation of NPM/B23, a question that emerges is which kinase phosphorylates NPM/B23, in ATM-depleted cells, leading to ARF stabilization. It is reported that DNA-damage-activated PP1 keeps Nek2A kinase turned off[32]. Nek2A is a cell-cycle kinase involved mainly in centrosome duplication[32]. As Nek2A interacts with NPM/B23 in the nucleoli[33], we examined whether Nek2A is the kinase responsible for phosphorylation of NPM/B23 (ref. 34) impacting ARF turnover. Indeed, ARF abundance was not increased in ATM-compromised cells with silenced *Nek2A*, strongly supporting the notion that upregulation of ARF in ATM-silenced cells is mediated through Nek2A activation (Fig. 3f).

Subsequently, we investigated which amino-acid residues of NPM/B23 are phosphorylated. To this end, a mass-spectrometry-based comparative phosphoproteome analysis was conducted revealing phosphorylation of NPM on Ser 70 in cells in which ATM or PP1 was inhibited, but not in cells treated with doxorubicin or those with depleted Nek2 (Fig. 4a,b and Supplementary Table and Note S1). Another Nek2-dependent phosphorylation was detected on Ser 88 of NPM (Fig. 4a,b and Supplementary Table and Note S1). These results suggest that phosphorylation of NPM by Nek2 on Ser 70 and Ser 88 is antagonized by PP1, when PP1 is activated by ATM.

To examine whether phosphorylation of Ser 70 and Ser 88 regulates the interaction of NPM/B23 with ARF, we substituted these serines with alanine or aspartic acid in myc-tagged NPM/B23 and examined binding of the mutant NPM/B23 proteins to endogenous ARF. The experiment was conducted in $NPM^{-/-}$ $p53^{-/-}$ MEFs to avoid interference with endogenous NPM/B23 (refs 22,23). The assay demonstrated an increase of ARF binding to S70D-NPM/B23 that was further enhanced in the context of S70/88D-NPM/B23 (Fig. 4c). Overall, our data unravel an ATM-dependent pathway that controls ARF protein stability by regulating the phosphorylation status of NPM/B23.

ATM-dependent ARF upregulation restrains ribosomal biogenesis and cell-cycle progression

To establish that the observed regulation of ARF levels by ATM is biologically significant, we examined whether ATM modulates known functions downstream of ARF. ARF has both p53-dependent and p53-independent functions[1]. As ATM directly regulates p53, we chose to study a p53-independent function of ARF, specifically suppression of ribosomal biogenesis[35,36]. The impact of ATM inhibition on ribosomal RNA (rRNA) biogenesis was analysed by quantitative RT–PCR and pulse-chase labelling of newly synthesized rRNA. RT–PCR assessment demonstrated that the levels of the precursor 47S rRNA, which reflect the rate of Pol-I transcription initiation, promoter escape and elongation[37], were reduced in ATMi cells and were rescued when *ARF* was concurrently silenced (Fig. 5a). In line with the qRT–PCR data, pulse-chase analysis showed from the beginning of chasing (0 min) that the synthesis of the precursor molecule 47S rRNA was suppressed, apparently affecting the processing of the rRNA intermediates. Silencing of *ARF* restored rRNA synthesis and maturation, suggesting that the effect of ATM inactivation is mediated by ARF (Fig. 5b and Supplementary Fig. S4). Within this context, it was recently reported that ARF hampers rRNA synthesis by obstructing the chaperone activity of NPM/B23 and sequestering the RNA polymerase I (Pol-I) transcription termination factor I (TTF-I)-NMP/B23 complex in the nucleoplasm[38]. Monitoring the distribution of NPM/B23 in ATMi cells, over time, we noticed its shuttling in the nucleoplasm, whereas its nucleolar fraction was concomitantly reduced, leaving the total levels of NPM/B23 stable (Supplementary Fig. S5a,b). The shuttling of NPM/B23 to the nucleoplasm was followed by increased ARF (Supplementary Fig. S5a–c) and Pol-I TTF-I levels (Supplementary Fig. S5a,c) in the nucleoplasm, as well, implying a deregulation in rRNA processing[39]. Likewise, *ARF* siRNA treatment of ATMi cells restored the shuttling of Pol-I TTF-I to the nucleolus (Supplementary Fig. S5c).

To validate the rRNA results, we implemented a multidimensional liquid chromatography–tandem mass spectrometry (LC–MS/MS) analysis using iTRAQ multiplex labelling[40,41] to obtain a global estimate of the proteome in the treated cells. Consistent with the rRNA analysis, inhibition of either ATM or PP1 caused suppression in the translation machinery network ($P < 0.0001$) as revealed by gene set enrichment analysis (see Fig. 5c and Supplementary Methods, Table S2 and Notes S1 and S6), whereas silencing of *ARF* rescued partially this outcome by mainly increasing the levels of the large ribosomal subunit proteins ($P = 0,008575$; Fig. 5c). Together, these results imply that within the context of inhibited/silenced ATM, ARF is upregulated hindering mainly rRNA synthesis and processing, and to a lesser extent ribosomal protein production.

ATM inactivation is linked to cell-cycle checkpoint defects and cell-cycle progression[42]. However, in cells that retain an intact *CDKN2A* locus, the increased ARF levels that accompany loss of ATM activity could result in delayed cell-cycle progression. Indeed, in proliferating H1299 and Saos2 cells, inactivation of ATM led to a significant growth delay that was rescued by ARF silencing (Fig. 6a,b), whereas suppression of ATM in A549 lung cancer cells, which are ARF-null, had no effect (Fig. 6a). In parallel, the mRNA and protein levels of

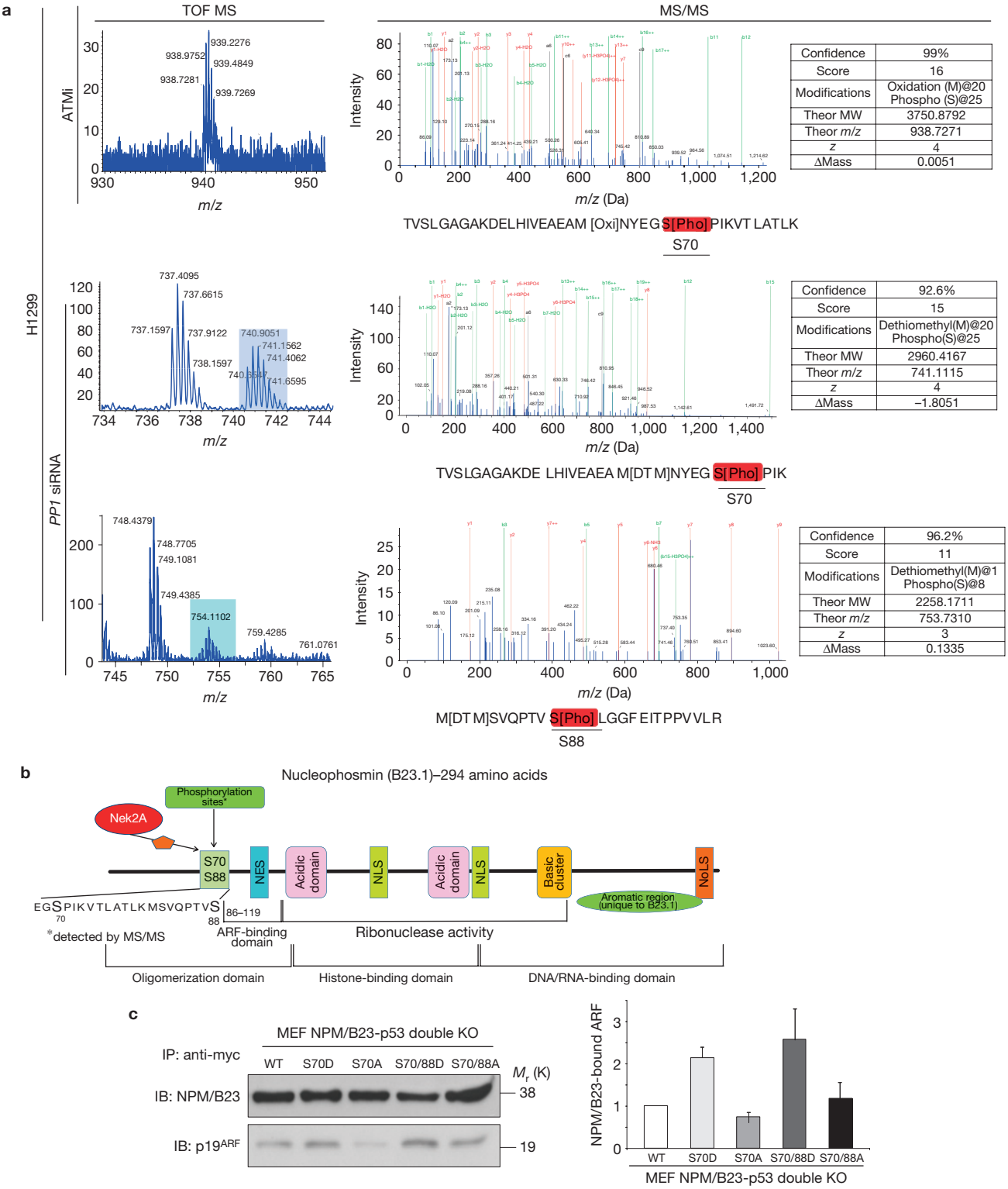

Figure 4 Phosphorylation of NPM/B23 at Ser 70 and Ser 88 enhances $p14^{ARF}$ protein stability. (**a**) LC–MS analysis followed by MS/MS of immunoprecipitated NPM/B23 from H1299 cells treated with Ku55933 (ATMi) and *PP1* siRNA revealing phosphorylation of Ser 70 and Ser 88 in ATMi cells. (**b**) Schematic structure depicting interaction and functional domains of NPM/B23. (**c**) Increased binding of $p19^{ARF}$ to myc-tagged immunoprecipitated (IP) phosphomimetic NPM/B23 mutants S70D and S70/88D compared with wild-type (WT) NPM/B23, in MEF KO NPM/*B23*$^{-/-}$ *p53*$^{-/-}$. Single or combined substitutions replacing serines with alanines (neutral), or aspartic acid residues (phosphomimetic) were employed. The histogram shows quantitative densitometry results of the corresponding immunoblot (IB, $P = 0.001$, *t*-test, error bars indicate s.d., $n = 5$ blots). Uncropped images of blots are shown in Supplementary Fig. S9.

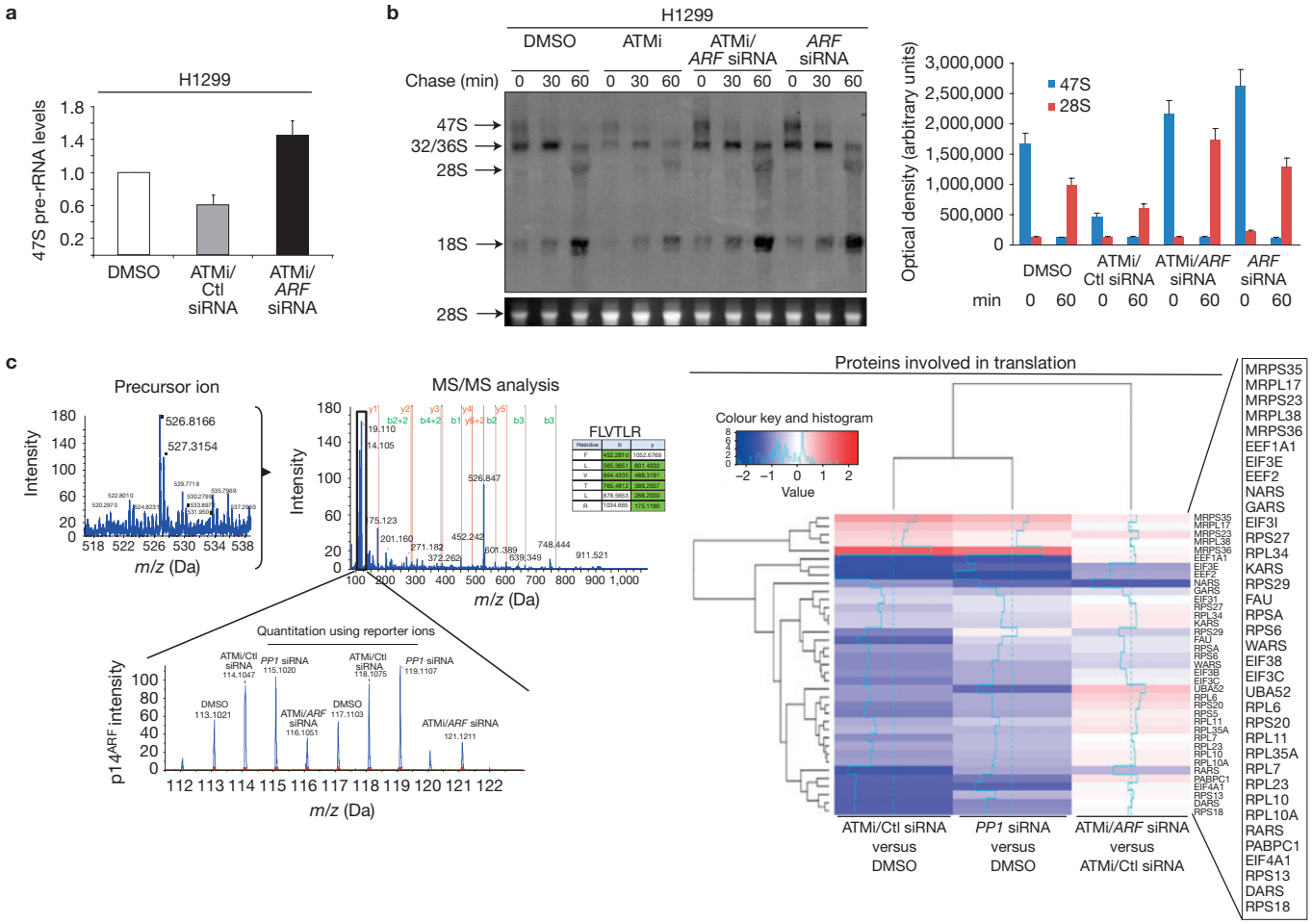

Figure 5 ATM-dependent p14^{ARF} regulation affects ribosomal biogenesis. (**a**) Real-time qRT–PCR analysis showing decreased mRNA levels of precursor 47S rRNA in ATMi, rescued on *ARF* siRNA. The histogram shows quantification of real-time RT–PCR ($P < 0.001$, *t*-test, error bars indicate s.d., $n = 4$ real-time RT–PCR runs). (**b**) Pulse-chase analysis of rRNA processing in DMSO-, ATMi-, ATMi/*ARF* siRNA- and *ARF* siRNA-treated H1299 cells, showing suppressed rRNA synthesis and processing in ATMi, rescued following *ARF* siRNA. Lower lane depicting ethidium bromide staining of 28S rRNA serves for equal loading. Bars represent densitometric analysis results ($P < 0.002$, pair-wise *t*-test, error bars indicate s.d.). (**c**) Precursor detection and MS/MS spectral evidence of a p14^{ARF} peptide identified from the whole proteome multidimensional quantitative LC–MS/MS analysis. The iTRAQ reporter ions showing the p14^{ARF} quantitative alterations across samples of different treatments are presented. The heat map (bottom right) depicts 37 identified proteins from the whole proteome analysis found to belong to the translation machinery network, most of which are suppressed by either ATMi or *PP1* siRNA treatments. A partial rescue of this outcome by p14^{ARF} silencing in ATM inhibited samples is also shown in the heat map, where ~50% of the proteins (among which all of the large ribosomal subunits, half of the small ribosomal subunit proteins and several translation initiation factors are included) exhibit an increase in their expression levels.

cyclin E were reduced in ATMi cells and were re-established after *ARF* siRNA (Fig. 6c). Consistent with a recent study demonstrating that ARF represses cyclin E transcription by mediating histone H2B Lys 20 deacetylation of its promoter[43], chromatin immunoprecipitation (ChIP) analysis in ATMi cells showed decreased H2B Lys 20 acetylation of the cyclin E promoter that was restored on silencing of ARF (Fig. 6d). Thus, these results suggest that ARF can compensate for some of the cell-cycle checkpoint defects arising from impaired ATM function.

In vivo evidence supporting the functional link between ATM and ARF

To verify the *in vivo* relevance of the findings described above, we examined the status of ATM and ARF in a panel of human lung carcinomas (Supplementary Fig. S7a). Lung carcinomas were chosen because of the high prevalence of *ATM* mutations and decreased ATM expression (Supplementary Fig. S7b, Table S3 and Note S2). The subset of carcinomas with reduced ATM protein levels had higher ARF levels and reduced phosphorylation of the I-2 PP1 regulatory subunit when compared with the carcinomas with intact ATM (Fig. 7a–c and Supplementary Fig. S7c). The inverse relationship between ATM and ARF was even stronger in the cases with high p16^{INK4A} expression (Fig. 7b), further strengthening the notion that decreased ARF, in this setting, is linked specifically with ATM activation and not aberrations in the *CDKN2A* locus.

The ATM–ARF pathway may be relevant in cancer development, because inhibition of ATM could boost the p53-independent tumour-suppressor activities of ARF (ref. 1). To this end, lentiviruses carrying specific shATM-silencing sequences (Supplementary Figs S4 and S8a) or the corresponding control (ctl shRNA) were injected intratumorally into H1299 xenografts. Expression of GFP in a significant proportion

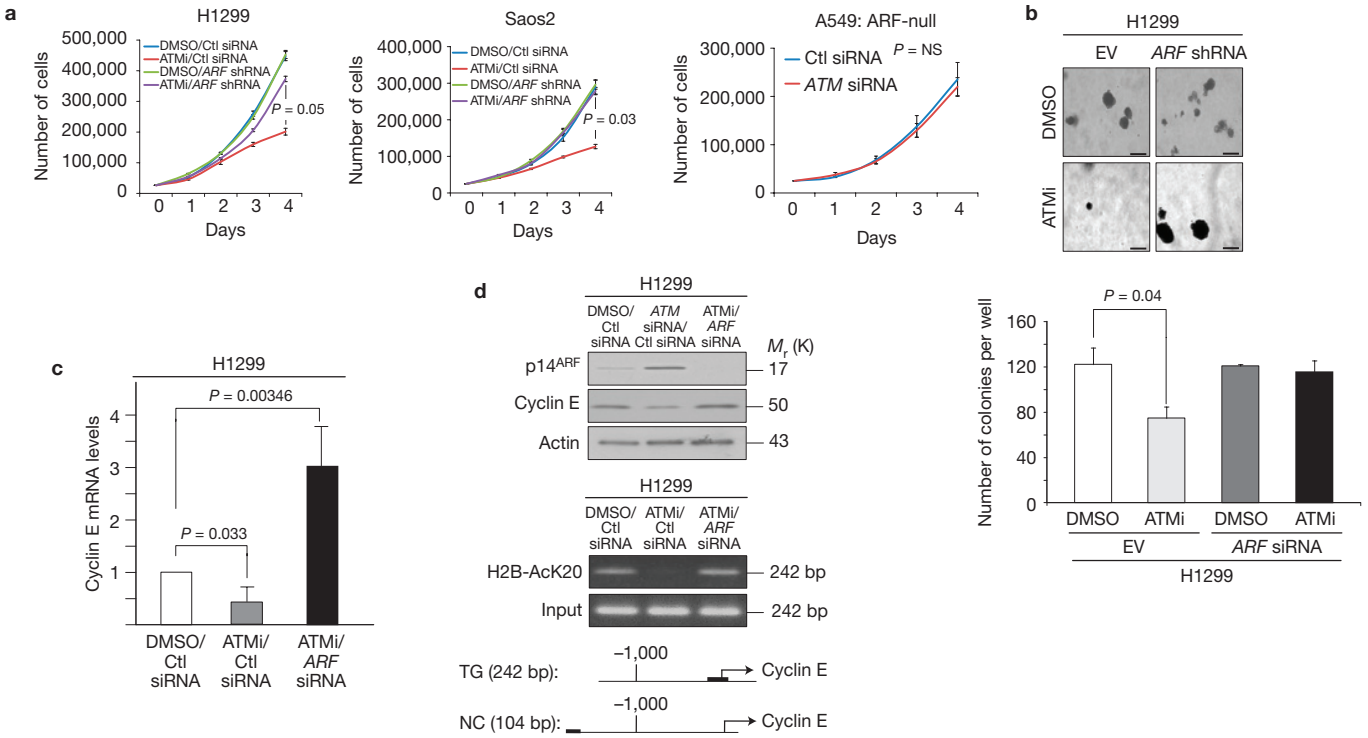

Figure 6 ATM-dependent p14^{ARF} regulation affects cell growth. (**a**) ATMi delayed growth in H1299 and Saos2 cells, restored in ATMi/*ARF* siRNA-treated cells. ATMi had no effect on the growth of ARF-null A549 cells (mean value from four repetitions, $P = 0.05$, $P = 0.03$ and $P =$ NS respectively, pair-wise *t*-test, error bars indicate s.d.). (**b**) Significant decrease in number of colonies in ATMi H1299 cells compared with control cells (DMSO). The effect is neutralized in ATMi/*ARF* shRNA cells. Mean values from four fields are plotted with s.d. ($P = 0.04$, *t*-test). Scale bars, 80 μm. EV, empty vector. (**c**) Real-time qRT–PCR demonstrates decreased cyclin E mRNA levels in ATMi H1299 cells, which are rescued on *ARF* siRNA treatment. Bar chart shows quantification of real-time RT–PCR (mean value from triplicates, $P = 0{,}033$ and $P = 0{,}003346$ respectively, pair-wise *t*-test, error bars indicate s.d., $n = 3$ real-time RT–PCR runs). (**d**) Immunoblot analysis showing decrease in cyclin E levels in siATM H1299 cells, which are restored on *p14^{ARF}* silencing. Similar results were obtained in ATMi H1299 cells. Actin served as loading control. ChIP analysis depicting hypo-acetylation of H2BK20 of the cyclin E promoter in ATMi cells, restored after *ARF* siRNA. TG, target ChIP amplicon (242 bp) in *cyclin E* promoter; NC, negative control ChIP amplicon (104 bp), located > 1,500 bp from the cyclin E transcription start site (experimental data not shown); ATMi, Ku55933 treatment; ctrsi, control siRNA; NS, not significant. Uncropped images of blots are shown in Supplementary Fig. S9.

of tumour cells confirmed successful delivery of the lentiviruses (Supplementary Fig. S8b,c). The intratumoral shRNA injections were performed for a period of four weeks (Supplementary Fig. S8d) either in the same animal (right flank: control, left flank: lenti-shATM; Fig. 8a) or in separate mice (Supplementary Fig. S8e). Results were identical in both cases and showed that inhibition of ATM reduced the size of H1299 xenografts forming in immunocompromised mice (Fig. 8a,b). This effect required ARF, because the size of H1299-shARF xenografts was unaffected by silencing ATM, and led to a more aggressive tumour behaviour (Fig. 8a,b). Similar results were obtained by treatment with caffeine[5], which inhibits ATM (ref. 44; Supplementary Fig. S8f–h). Further, in human lung carcinomas, in which the status of the *TP53* gene had already been characterized[45,46], cyclin E expression and the proliferation index (Ki67) of p53 negative/mutant lung carcinomas with decreased ATM levels and high ARF expression was significantly lower when compared with those with normal ATM levels (Fig. 8c,d).

DISCUSSION

Taken together, our present data provide new insights into the orchestration of the DDR and ARF as intrinsic barriers against progression of human cancer. The *in vitro* and *in vivo* data identify a pathway connecting ATM activation with ARF protein suppression. Specifically, we propose that ATM activates the PP1 phosphatase, which counteracts the Nek2-dependent phosphorylation of NPM/B23 at Ser 70 and Ser 88, thereby leading to stabilization of ARF. PP1-dependent dephosphorylation of NPM/B23 weakens ARF binding to NPM/B23, and the released ARF is then targeted for ULF-mediated degradation. Thus, inhibition of ATM enhances ARF levels and thus promotes p53-dependent and -independent anti-tumour functions of ARF (Fig. 8e). The present study also helps to reconcile previous results indicating that ARF is regulated in a DNA-damage-independent manner[9,11]. Our study suggests that although ARF mRNA levels are indeed regulated in a DDR-independent manner, there is a cross-talk between DDR signalling and ARF protein turnover. Hence, two signalling routes lead to ARF induction: oncogenic challenge[1] and ATM suppression. Given that oncogenes activate ATM, as well[4,6], it seems that oncogenic insults trigger two pathways that regulate ARF levels (Supplementary Fig. S1j). Although at first sight the oncogene–ARF and ATM–ARF pathways seem antagonistic, they actually form a regulatory network that functions as a safe-guard mechanism, when ATM is inactivated, by boosting ARF levels. The

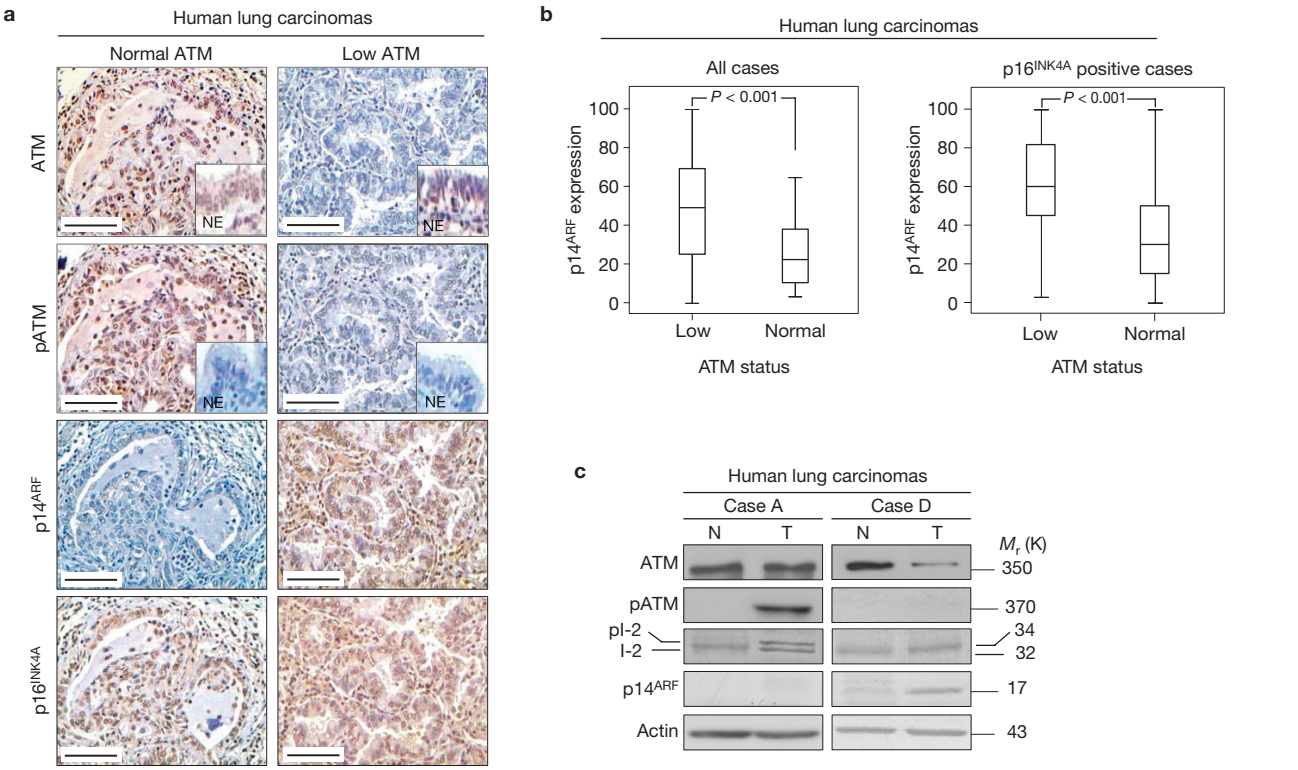

Figure 7 ATM abrogation is inversely related to ARF expression in lung cancer. (**a**) Serial immunohistochemical analysis of total ATM (ATM), phospho-ATM (p-ATM), $p14^{ARF}$ and $p16^{INK4A}$ in non-small cell lung carcinomas. Insets depict corresponding normal tissues serving as a positive control for total ATM and negative control for p-ATM expression in a case with ATM loss in the tumour area and no ATM activation in the normal tissue. Scale bars, 100 μm. (**b**) Box plots showing that $p14^{ARF}$ expression—as examined by immunohistochemistry—was statistically higher in cases with decreased ATM protein levels (analysis of variance, $n = 121$ cases). This association was even stronger in the $p16^{INK4A}$-positive group (analysis of variance, $n = 79$ cases), denoting that this relationship is not attributed to loss or epigenetic silencing of the *CDKN2A* locus. (**c**) Immunoblot analysis in two representative lung carcinomas with normal and low ATM levels, respectively. In the first case p-ATM expression was accompanied by phospho-I-2 (pI-2) and absence of $p14^{ARF}$ expression, whereas the second case reveals decreased ATM, along with no pI-2 and increased $p14^{ARF}$ levels. Actin served as loading control. Uncropped images of blots are shown in Supplementary Fig. S9.

oncogene–ATM–ARF network bears similarities to the regulatory loop involving p53–ARF, in which p53 negatively regulates ARF (refs 10,47). In the latter case abrogation of p53 leads to enhanced ARF expression that could compensate at least partially for p53 loss by triggering its p53-independent anti-proliferative functions. Moreover, it was recently shown that p53-deficient cells are sensitized to DNA-damage-mediated mitotic catastrophe by ATM inhibition[48]. Within this context it was demonstrated that breast cancer patients with ATM-low/p53-mutant tumours survived longer after chemotherapy when compared with patients whose tumours exhibited normal ATM levels and aberrant/mutant p53. Although the mechanism suggested by the authors may explain this outcome, it is also plausible that the ATM–ARF pathway studied here (Fig. 8e) could have contributed to the observed delayed tumour growth, and hence better survival in the group of patients with tumours featuring low ATM and inactive p53.

Despite the suggested limited tumour-suppressive role of ATM in mice[13] and the differences in ARF regulation between humans and mice[49], the ATM–ARF pathway may possibly play a role in certain types of murine malignancy, such as fibrosarcomas[11]. Within this context, the increased levels of ARF noticed in ATM-null MEFs when compared with wild-type ones[11,49] can also be explained by this mechanistic link, especially in view of recent data demonstrating that MEFs cultured under standard conditions exhibit an activated DDR pathway[50]. In support to this notion, ARF expression was abolished in irradiated wild-type ATM MEFs but not in ATM-null MEFs (Supplementary Fig. S8i). Furthermore, ATM may regulate ARF turnover also in spermatogonia, possibly the only scenario where ARF is expressed under physiological conditions[51] and is found increased in $ATM^{-/-}$ testis[52]. Indeed, we found that ARF protein, but not mRNA, was downregulated in normal mouse spermatogonia when ATM was activated on exposure to ionizing radiation *in vivo* (Supplementary Fig. S8j).

There are few reports suggesting that ARF contributes to the DDR signalling cascade, as well[53–55]. Although such conclusions were mostly based on experiments using forced expression of ARF we cannot exclude the possibility that a bidirectional relationship between DDR and ARF exists. In this scenario increased expression of ARF due to ATM suppression would form a positive feedback loop to enhance the remaining active DDR signalling routes such as the ATR/Chk1 pathway[54].

In conclusion and from a clinical perspective, the evidence provided here suggests that ATM and ARF form a tightly regulated network and supports the role of ARF as an important secondary anti-tumour response that becomes particularly robustly activated when ATM is lost or otherwise disabled during tumour progression. □

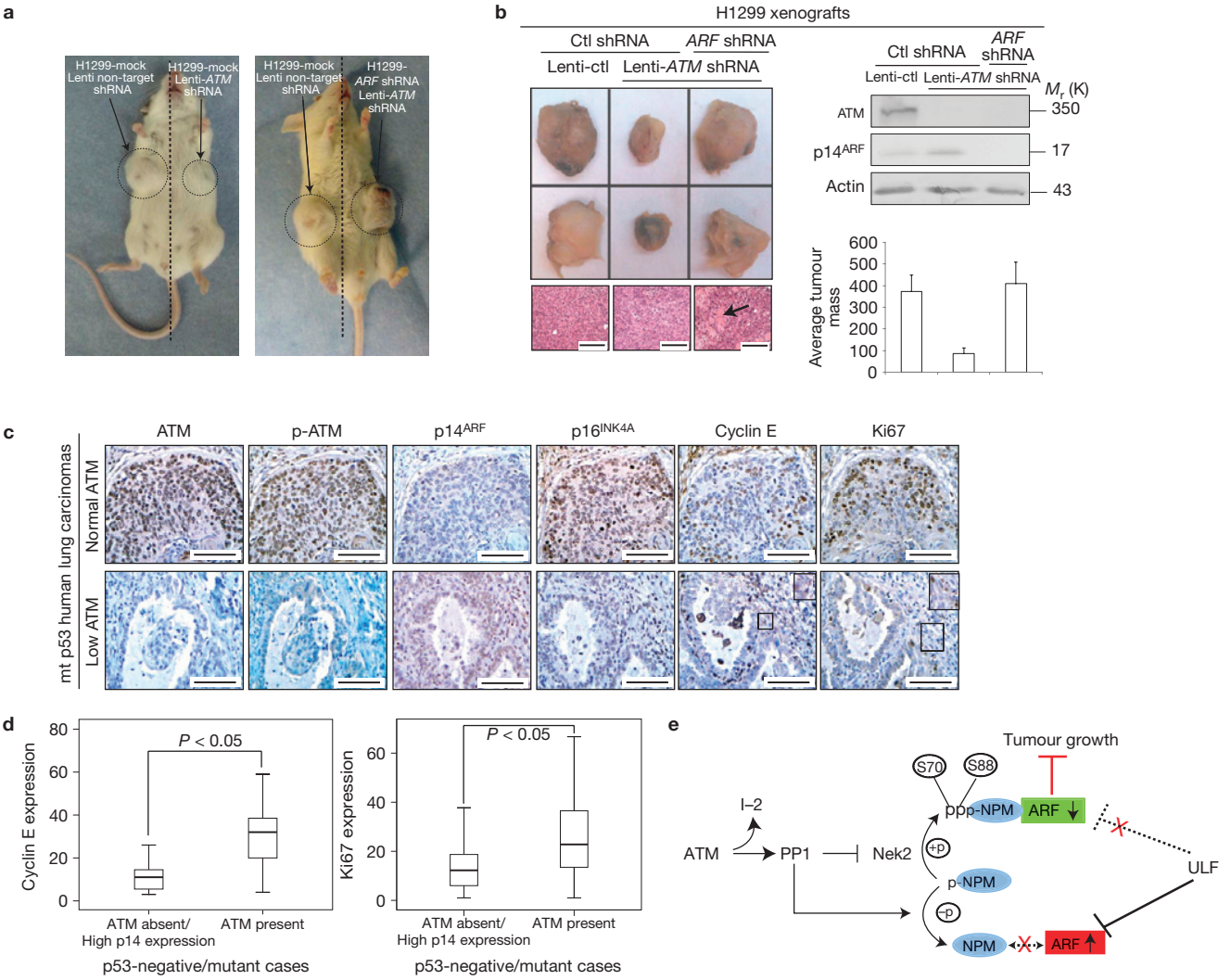

Figure 8 ATM abrogation stalls growth in p53-null xenografts in an ARF-dependent manner. (**a**) Tumours produced in immunocompromised mice engrafted with mock (ctl shRNA) H1299 cells and injected with lenti-*ATM* shRNA (right tumour in left panel animal) in comparison with H1299 shARF cells injected with lenti-*ATM* shRNA (right tumour in right panel animal; see also Supplementary Fig. S8a–d). (**b**) Tumours generated from grafted H1299 cells exhibited a significantly reduced size after suppression of ATM (*ATM* shRNA), but remained unaffected in size when ATM suppression (*ATM* shRNA) was performed in H1299 shARF xenografts. Haematoxylin–eosin sections from the developed tumours (black arrow depicts invasion of abdominal wall muscle layer). Immunoblot analysis depicting the $p14^{ARF}$ protein levels in the control (GFP), *ATM* shRNA and *ATM/ARF*-shRNAs tumours. Histogram presents the average mass between the groups of generated tumours ($P = 0.007$, *t*-test, error bars indicate s.d., $n = 30$ tumours). Scale bars, 200 μm. (**c**) Serial images from comparative immunohistochemical analysis of ATM, $p14^{ARF}$, $p16^{INK4A}$, cyclin E and Ki-67 markers in lung cancer cases with mutant p53, stratified according to ATM expression status (low versus normal). Dashed rectangular areas are magnified in insets. Scale bars, 100 μm. (**d**) Box plots depict cyclin E expression and proliferation index, as assessed by Ki-67 staining, in mutant p53 non-small cell lung carcinoma cases with decreased ATM protein levels and high $p14^{ARF}$ expression compared with cases with normal ATM status (analysis of variance, $n = 83$ cases). (**e**) Proposed model depicting the ATM–PP1–Nek2–NPM/B23 pathway that regulates ARF protein stability (see text). Actin served as loading control. Ctl, control. Uncropped images of blots are shown in Supplementary Fig. S9.

METHODS

Methods and any associated references are available in the online version of the paper.

Note: Supplementary Information is available in the online version of the paper

ACKNOWLEDGEMENTS

We would like to thank G. Peters (Cancer Research UK London Research Institute, UK), D. Ginsberg (Bar Ilan University, Israel), P. G. Pelicci (European Institute of Oncology, Italy; University of Milan, Italy), M. Serrano (Spanish National Cancer Research Centre, Spain), Y. Shiloh (Tel Aviv University, Israel) and K. Vousden (Cancer Research-UK, Beatson Institute, UK) for providing reagents for this work. Special thanks for expert technical support from A. Damalas on the BJ cell treatments with serum starvation and T. Liloglou for manipulations with the HBECs and their derivatives. Financial support was from the European Commission FP7 (projects GENICA, INFLA-CARE, BioMedReg, DDResponse and INsPiRE), the Danish Cancer Society, and the Danish National Research Foundation. G.V. is a recipient of a Hellenic Association for Molecular Cancer Research scholarship. Dr A. Kotsinas is a recipient of an Empeirikeion Foundation fellowship. This work is dedicated to the memory of G. V. Gorgoulis.

AUTHOR CONTRIBUTIONS

G.V. and M.L.: cell culture and manipulations, siRNA/plasmid/viral transfections/transductions/infections, ubiquitination assay, western blots, cell growth analyses and soft agar assays. K.V., T.R. and V.G.G.: proteomic analysis design and experimentation. E.K., J. Bartkova, I.S.P. and J. Bartek: human and mouse pathological evaluations, immunohistochemical analyses and evaluations, and tu-

mour immunofluorescence analyses. A.K.: real-time (RT-)PCR analyses. M.S.: ChIP assay. M.S. and G.V.: rRNA pulse-chase analysis, immunoprecipitation analyses, plasmid and lentiviral production. A.D-O., M.K. and T.D.H.: I-2 mutagenesis analyses and corresponding immunofluorescence and western blot analyses. I.O., S.B., M.C-B. and S.V.: nuclear fractionation, nucleolar immunofluorescence and western blot analyses, NPM site-directed mutagenesis and 47S pre-rRNA real-time RT–PCR analysis. V.Z., D.K., G.P., A. Klinakis and V.G.G.: xenografts and mice manipulations. K.V., M.L. and A. Kotsinas: Bioinformatic and statistical analyses. W.G.: data analysis and production of reagents. J. Bartek and T.D.H.: data analysis and interpretation, and assistance in manuscript preparation. VG.: experimental design, guidance, manuscript preparation and writing.

COMPETING FINANCIAL INTERESTS

The authors declare no competing financial interests.

Published online at www.nature.com/doifinder/10.1038/ncb2795
Reprints and permissions information is available online at www.nature.com/reprints

1. Sherr, C. J. Divorcing ARF and p53: an unsettled case. *Nat. Rev. Cancer* **6,** 663–673 (2006).
2. Kim, W. Y. & Sharpless, N. E. The regulation of INK4/ARF in cancer and aging. *Cell* **127,** 265–275 (2006).
3. Bartek, J., Bartkova, J. & Lukas, J. DNA damage signalling guards against activated oncogenes and tumour progression. *Oncogene* **26,** 7773–7779 (2007).
4. Halazonetis, T. D., Gorgoulis, V. G. & Bartek, J. An oncogene-induced DNA damage model for cancer development. *Science* **319,** 1352–1355 (2008).
5. Jackson, S. P. & Bartek, J. The DNA-damage response in human biology and disease. *Nature* **461,** 1071–1078 (2009).
6. Negrini, S., Gorgoulis, V. G. & Halazonetis, T. D. Genomic instability–an evolving hallmark of cancer. *Nat. Rev. Mol. Cell Biol.* **11,** 220–228 (2010).
7. Hanahan, D. & Weinberg, R. A. Hallmarks of cancer: the next generation. *Cell* **144,** 646–674 (2011).
8. Kastan, M. B. & Bartek, J. Cell-cycle checkpoints and cancer. *Nature* **432,** 316–323 (2004).
9. Kamijo, T. *et al.* Tumor suppression at the mouse INK4a locus mediated by the alternative reading frame product p19ARF. *Cell* **91,** 649–659 (1997).
10. Stott, F. J. *et al.* The alternative product from the human CDKN2A locus, p14ARF, participates in a regulatory feedback loop with p53 and MDM2. *EMBO J.* **17,** 5001–5014 (1998).
11. Kamijo, T. *et al.* Loss of the ARF tumor suppressor reverses premature replicative arrest but not radiation hypersensitivity arising from disabled atm function. *Cancer Res.* **59,** 2464–2469 (1999).
12. Shiloh, Y. ATM and related protein kinases: safeguarding genome integrity. *Nat. Rev. Cancer* **3,** 155–168 (2003).
13. Efeyan, A. *et al.* Limited role of murine ATM in oncogene-induced senescence and p53-dependent tumor suppression. *PLoS One* **4,** e5475 (2009).
14. Hickson, I. *et al.* Identification and characterization of a novel and specific inhibitor of the ataxia-telangiectasia mutated kinase ATM. *Cancer Res.* **64,** 9152–9159 (2004).
15. DiTullio, R. A. Jr *et al.* 53BP1 functions in an ATM-dependent checkpoint pathway that is constitutively activated in human cancer. *Nat. Cell Biol.* **12,** 998–1002 (2002).
16. Tsantoulis, P. K. & Gorgoulis, V. G. Involvement of E2F transcription factor family in cancer. *Eur. J. Cancer* **41,** 2403–2414 (2005).
17. Liontos, M. *et al.* Modulation of the E2F1-driven cancer cell fate by the DNA damage response machinery and potential novel E2F1 targets in osteosarcomas. *Am. J. Pathol.* **175,** 376–391 (2009).
18. Ramirez, R. D. *et al.* Immortalization of human bronchial epithelial cells in the absence of viral oncoproteins. *Cancer Res.* **64,** 9027–9034 (2004).
19. Sato, M. *et al.* Multiple oncogenic changes (K-RAS(V12), p53 knockdown, mutant EGFRs, p16 bypass, telomerase) are not sufficient to confer a full malignant phenotype on human bronchial epithelial cells. *Cancer Res.* **66,** 2116–2128 (2006).
20. Inoue, R., Asker, C., Klangby, U., Pisa, P. & Wiman, K. G. Induction of the human ARF protein by serum starvation. *Anticancer Res.* **19,** 2939–2943 (1999).
21. Chen, D., Shan, J., Zhu, W. G., Qin, J. & Gu, W. Transcription-independent ARF regulation in oncogenic stress-mediated p53 responses. *Nature* **464,** 624–627 (2010).
22. Enomoto, T., Lindstrom, M. S., Jin, A., Ke, H. & Zhang, Y. Essential role of the B23/NPM core domain in regulating ARF binding and B23 stability. *J. Biol. Chem.* **281,** 18463–18472 (2006).
23. Colombo, E. *et al.* Nucleophosmin is required for DNA integrity and p19Arf protein stability. *Mol. Cell. Biol.* **25,** 8874–8886 (2005).
24. Kuo, M. L., den Besten, W., Bertwistle, D., Roussel, M. F. & Sherr, C. J. N-terminal polyubiquitination and degradation of the Arf tumor suppressor. *Genes Dev.* **18,** 1862–1874 (2004).
25. Huang, M., Itahana, K., Zhang, Y. & Mitchell, B. S. Depletion of guanine nucleotides leads to the Mdm2-dependent proteasomal degradation of nucleostemin. *Cancer Res.* **69,** 3004–3012 (2009).
26. Lee, C., Smith, B. A., Bandyopadhyay, K. & Gjerset, R. A. DNA damage disrupts the p14ARF-B23 (nucleophosmin) interaction and triggers a transient subnuclear redistribution of p14ARF. *Cancer Res.* **65,** 9834–9842 (2005).
27. Matsuoka, S. *et al.* ATM and ATR substrate analysis reveals extensive protein networks responsive to DNA damage. *Science* **316,** 1160–1166 (2007).
28. Lin, C. Y. *et al.* Dephosphorylation of nucleophosmin by PP1 β facilitates pRB binding and consequent E2F1-dependent DNA repair. *Mol. Biol. Cell* **21,** 4409–4417 (2010).
29. Tang, X. *et al.* A novel ATM-dependent pathway regulates protein phosphatase 1 in response to DNA damage. *Mol. Cell. Biol.* **28,** 2559–2566 (2008).
30. Scheer, U. & Benavente, R. Functional and dynamic aspects of the mammalian nucleolus. *Bioessays* **12,** 14–21 (1990).
31. Trinkle-Mulcahy, L., Sleeman, J. E. & Lamond, A. I. Dynamic targeting of protein phosphatase 1 within the nuclei of living mammalian cells. *J. Cell Sci.* **114,** 4219–4228 (2001).
32. Hayward, D. G. & Fry, A. M. Nek2 kinase in chromosome instability and cancer. *Cancer Lett.* **237,** 155–166 (2006).
33. Noguchi, K., Fukazawa, H., Murakami, Y. & Uehara, Y. Nucleolar Nek11 is a novel target of Nek2A in G1/S-arrested cells. *J. Biol. Chem.* **279,** 32716–32727 (2004).
34. Colombo, E., Alcalay, M. & Pelicci, P. G. Nucleophosmin and its complex network: a possible therapeutic target in hematological diseases. *Oncogene* **30,** 2595–2609 (2011).
35. Sugimoto, M., Kuo, M. L., Roussel, M. F. & Sherr, C. J. Nucleolar Arf tumor suppressor inhibits ribosomal RNA processing. *Mol. Cell* **11,** 415–424 (2003).
36. Itahana, K. *et al.* Tumor suppressor ARF degrades B23, a nucleolar protein involved in ribosome biogenesis and cell proliferation. *Mol. Cell* **12,** 1151–1164 (2003).
37. Grandori, C. *et al.* c-Myc binds to human ribosomal DNA and stimulates transcription of rRNA genes by RNA polymerase I. *Nat. Cell Biol.* **7,** 311–318 (2005).
38. Lessard, F. *et al.* The ARF tumor suppressor controls ribosome biogenesis by regulating the RNA polymerase I transcription factor TTF-I. *Mol. Cell* **38,** 539–550 (2010).
39. Huang, M., Ji, Y., Itahana, K., Zhang, Y. & Mitchell, B. Guanine nucleotide depletion inhibits pre-ribosomal RNA synthesis and causes nucleolar disruption. *Leuk. Res.* **32,** 131–141 (2008).
40. Cox, J. & Mann, M. Quantitative, high-resolution proteomics for data-driven systems biology. *Annu. Rev. Biochem.* **80,** 273–299 (2011).
41. Li, Z. *et al.* Systematic comparison of label-free, metabolic labeling, and isobaric chemical labeling for quantitative proteomics on LTQ Orbitrap Velos. *J. Proteome. Res.* **11,** 1582–1590 (2012).
42. Falck, J., Mailand, N., Syljuasen, R. G., Bartek, J. & Lukas, J. The ATM-Chk2—Cdc25A checkpoint pathway guards against radioresistant DNA synthesis. *Nature* **410,** 842–847 (2001).
43. Choi, J. *et al.* Selective requirement of H2B N-Terminal tail for p14ARF induced chromatin silencing. *Nucleic. Acids Res.* **39,** 9167–9180 (2011).
44. Sarkaria, J. N. *et al.* Inhibition of ATM and ATR kinase activities by the radiosensitizing agent, caffeine. *Cancer Res.* **59,** 4375–4382 (1999).
45. Gorgoulis, V. G. *et al.* Alterations of the p16-pRb pathway and the chromosome locus 9p21-22 in non-small-cell lung carcinomas: relationship with p53 and MDM2 protein expression. *Am. J. Pathol.* **153,** 1749–1765 (1998).
46. Gorgoulis, V. G. *et al.* Activation of the DNA damage checkpoint and genomic instability in human precancerous lesions. *Nature* **434,** 907–913 (2005).
47. Zeng, Y., Kotake, Y., Pei, X. H., Smith, M. D. & Xiong, Y. p53 binds to and is required for the repression of Arf tumor suppressor by HDAC and polycomb. *Cancer Res.* **71,** 2781–2792 (2011).
48. Jiang, H. *et al.* The combined status of ATM and p53 link tumor development with therapeutic response. *Genes Dev.* **23,** 1895–1909 (2009).
49. Gorgoulis, V. G. & Halazonetis, T. D. Oncogene-induced senescence: the bright and dark side of the response. *Curr. Opin. Cell Biol.* **22,** 816–827 (2010).
50. Di Micco, R. *et al.* DNA damage response activation in mouse embryonic fibroblasts undergoing replicative senescence and following spontaneous immortalization. *Cell Cycle* **7,** 3601–3606 (2008).
51. Churchman, M. L., Roig, I., Jasin, M., Keeney, S. & Sherr, C. J. Expression of ARF tumor suppressor in spermatogonia facilitates meiotic progression in male germ cells. *Plos Genetics* **7,** e1002157 (2011).
52. Takubo, K. *et al.* Stem cell defects in ATM-deficient undifferentiated spermatogonia through DNA-induced cell-cycle arrest. *Cell Stem. Cell* **2,** 170–182 (2008).
53. Li, Y. *et al.* ATM activity contributes to the tumor-suppressing functions of p14ARF. *Oncogene* **23,** 7355–7365 (2004).
54. Eymin, B. *et al.* p14ARF activates a Tip60-dependent and p53-independent ATM/ATR/CHK pathway in response to genotoxic stress. *Mol. Cell Biol.* **26,** 4339–4350 (2006).
55. Khan, S. H., Moritsugu, J. & Wahl, G. M. Differential requirement for p19ARF in the p53-dependent arrest induced by DNA damage, microtubule disruption, and ribonucleotide depletion. *Proc. Natl Acad. Sci. USA* **97,** 3266–3271 (2000).

DOI: 10.1038/ncb2795

METHODS

Antibodies. A list of antibodies employed is provided in Supplementary Table S5.

Cell culture and treatments. Cell lines used were: H1299 (human non-small cell lung carcinoma cell line), HeLa (human cervix carcinoma cell line), HBEC (human bronchial epithelial cells) immortalized by hTERT/Cdk4 expression and K-Ras^{V12}-transfected immortalized HBECs, BJ (human diploid fibroblasts), Saos2 (human osteosarcoma cell line), MEFs and MEFs-*ATM*$^{-/-}$ (mouse embryo fibroblasts, donated by Y. Shiloh), NPM/B23-p53 double-KO MEFs (donated by P.G. Pelicci), NARF2 (p14^{ARF}-inducible osteosarcoma cell line derived from U2OS cells, donated by G. Peters; ref. 10) and Saos2 E2F1-ER cells (an E2F1-inducible system derived from Saos2 osteosarcoma cells, donated by D. Ginsberg; ref. 61).

With the exception of HBECs, cells were maintained in Dulbecco's modified Eagle's medium (DMEM; #41966, Invitrogen), supplemented with 10% FCS (#10270106, Invitrogen) and 100 μg ml^{-1} penicillin and streptomycin (#15070, Invitrogen), at 37 °C and 5% CO_2 (refs 58,59). For HBECs culture, keratinocyte serum-free medium (#17005-075, Invitrogen) was used supplemented with 50 μg ml^{-1} bovine Pituitary extract and 5 ng ml^{-1} hEGF (#17005-075, Invitrogen; refs. 18,19).

NARF2 cells were induced with 0.1 mM IPTG (#AM9462, Ambion), and Saos2 ER-E2F1 were induced with 300 nM 4-OH-tamoxifen (#579002, Calbiochem MERCK).

Cells at 80% confluency were treated with 10 μM ATM inhibitor (Ku55933, #118500, Calbiochem, MERCK; ref. 14), 2 μM doxorubicin (Adriblastina, Pfizer), 1 μM tautomycetin[56], (#2305, Tocris) or DMSO as a vehicle control for 24 h and then specific cells were treated with 10 μg ml^{-1} cycloheximide (#A0879, Applichem) for the time points indicated. H1299 cells were 10 Gy irradiated as previously described[57].

For immunofluorescence analysis, cells were cultured on coverslips and fixed with either frozen methanol for 5 min or in 4% formaldehyde and permeabilized with 0.1% Triton X-100 (#9002-93-1, Sigma) in two consecutive steps, each for 15 min at room temperature[58]. GFP-transfected cells grown on coverslips were fixed with 4% paraformaldehyde in PBS for 15 min and subsequently permeabilized with 0.5% Triton-X (#9002-93-1, Sigma) in PBS for 10 min.

***In vitro* mutagenesis and sequencing.** Full-length NPM/B23 cDNA in plasmid pRK5–Myc was used as a template for *in vitro* mutagenesis. Site-directed mutagenesis was carried out using the Change-IT Multiple Mutation Site Directed Mutagenesis Kit (Affymetrix, USB Products) and primers containing specific mutations (see Supplementary Table S6). After PCR-based mutagenesis products were digested twice with DpnI enzyme and *Escherichia coli* cells were transformed. For each mutation four clones were selected at random and were allowed to propagate overnight in an orbital shaker at 37 °C/ 250 r.p.m. in 3 ml Luria Bertani media supplemented with 100 μg ml^{-1} of ampicillin (#A7492, Applichem). Plasmid DNA was isolated using the PrepEase Mini Spin Plasmid Kit (Affymetrix, USB Products). Isolated plasmid DNAs were sequenced direct with the ABI BigDye Terminator ready reaction cycle sequencing kit v3.1 (Applied Biosystems) using CMV-F and SV40pA-R primers (see Supplementary Table S6) on an Applied Biosystems 3130 DNA Analyser (Applied Biosystems). Sequencing data were analysed with Sequencer 5 DNA sequence analysis software (Gene Codes).

Plasmids and siRNA transfection, retrovirus construction and infections. pRK5–Myc cloned NPM/B23 mutants (see Supplementary Table S4), pSNV2–GFP–ppp1r2h, pSNV2–GFP–ppp1r2hS43A and pSNV2–GPF–ppp1r2hS43D (ref. 62) were transfected into H1299 cells grown on coverslips, using the Effectene Transfection Reagent (#301425, Qiagen). Forty-eight hours after transfection, cells were fixed, as previously described, and stored for further immunofluorescence analysis[58]. BJ, H1299 and HeLa cells grown on DMEM complete medium without tetracycline traces were plated in 60 mm Petri dishes at a density of 1.2×10^5 cells per plate. Twenty-four hours later cells were transfected with either control siRNA (#12935–300, Stealth RNAi Negative Control Med GC, Invitrogen), ATM-specific siRNA duplexes (Stealth Select RNAi (set of 3 oligonucleotides #1299003), Invitrogen), *Chk2*-specific siRNA duplexes (Validated Stealth RNAi siRNA, Invitrogen), NPM/B23-specific siRNA (Stealth Select RNAi (set of 3 oligonucleotides, #1299003), Invitrogen), *ULF*-specific siRNA (Stealth Select RNAi (set of 3 oligonucleotides, #1299003), Invitrogen), *Nek2*-specific siRNA (Stealth Select RNAi (set of 3 oligonucleotides #1299003), Invitrogen) or *PP1*-isoform-specific siRNA (Stealth Select RNAi (set of 3 oligonucleotides #1299003), Invitrogen; ref. 31) using Lipofectamine 2000 (#11668027, Invitrogen; ref. 59). Cells were collected 48 h after transfection for further analysis. In β-catenin-infected BJ cells, transfection with either control or *ATM*-specific siRNA was repeated twice at 3-day intervals to ensure complete silencing of ATM during the experimental procedure.

BJ cells were transiently infected with the pBabe–β-catenin and the corresponding control vector using the Phoenix helper-free retrovirus producer cell line as previously described[59]. In brief, 70% confluent Phoenix cells were transfected, using the Lipofectamine 2000 transfection reagent, with β-catenin-expressing vector or the control vector alone, and the obtained replication-incompetent retroviruses were used for the transduction of BJ cells. The next day, after infection, the cells were selected with the appropriate antibiotic for 2 days and collected for further analysis 2 days later. H1299 cells were infected using the same protocol with the pBabe–H-Ras^{V12} and the corresponding control vector.

Total protein extraction, cell fractionation and immunoblotting. Total protein and histone extraction was performed according to protocols described elsewhere[59]. Cytoplasm, nuclei and nucleoli were prepared from 4×10^6 H1299 cells as previously described[63]. Signal development was performed with nitro blue tetrazolium/5-bromo-4-chloro-3-indolylphosphate (NBT/BCIP) solution (Invitrogen) or with chemiluminescent substrate ECL for HRP (#32106, Thermo Scientific). Blot quantifications were performed with ImageJ software.

Immunofluorescence analysis. Immunofluorescence analysis was performed as described previously[58,59]. Secondary anti-rabbit antibody conjugated with Texas red (#T2767, Texas red, Invitrogen) and secondary anti-mouse antibodies conjugated with Oregon green 488 (#O6380, Invitrogen) were used at 1:1,000 dilution for 45 min at 37 °C. Slides were analysed using an LSM700 confocal microscope (Zeiss) or a Zeiss Axioplan 2 fluorescence microscope. A minimum of 10 independent optical fields per sample section were counted and each sample was repeated minimum 3 times.

Immunoprecipitation. Cells treated with ATM inhibitor (Ku55933, MERCK) or doxorubicin for 24 h, as previously described, were lysed in RIPA buffer (Tris–HCl at pH 8.0, 50 mM, NaCl 150 mM, SDS 0.1%, sodium deoxycholate 1%, Triton X-100 1%, protease inhibitor cocktail (Thermo Scientific) and phosphatase inhibitor cocktail (Thermo Scientific)). Protein lysates were precleared with protein G agarose beads (Millipore) for 1 h and then incubated with G-protein beads bound to B23/NPM (Santa Cruz), anti-myc-tag or p14^{ARF} rabbit polyclonal antibody (donated by K. Vousden) for 2 h at 4 °C. Beads were washed 3 times in RIPA buffer. Protein was eluted from beads with 2xSDS-β-mercaptoethanol sample buffer, boiled for 8 min and then loaded on polyacrylamide gels for SDS–PAGE as described above. Blots were blocked in BSA 5% (for phosphor antibodies) or non-fat dry milk 5% in TBS–Tween 0.1% for 1 h and then incubated with primary antibody as described in the immunoblotting section.

***In vivo* ubiquitin assay.** For ubiquitin assay cells were treated with Ku55933 ATM inhibitor or doxorubicin for 24 h and with MG-132 proteasome inhibitor (#133407-82-6, MERCK) for 3 h at 30 μM. Cells were then lysed in RIPA buffer (Tris–HCl at pH 8.0, 50 mM, NaCl 150 mM, SDS 0.1%, sodium deoxycholate 1%, Triton X-100 1% and protease (#58440, Pierce, Thermo Scientific), phosphatase (#78420, Pierce, Thermo Scientific) inhibitor cocktail and *N*-ethylameleimide deubiquitinase inhibitor (#A2251, Applichem). Protein lysates were precleared with protein G agarose beads (#16-266, Millipore) for 1 h and then incubated with G-protein beads bound to p14^{ARF} rabbit polyclonal antibody for 2 h at 4 °C. Beads were washed 3 times in RIPA buffer containing protease, phosphatase and deubiquitinase inhibitors, as above. Protein was eluted from beads with 2xSDS-β-mercaptoethanol sample buffer, boiled for 8 min and then loaded on polyacrylamide gels for SDS–PAGE as described above. Blots were blocked for 1 h in 5% BSA in TBS–0.1% (v/v) Tween-20 solution at room temperature. Subsequently, membranes were incubated overnight with anti-ubiquitin antibody in 5% BSA in TBS supplemented with 0.1% (v/v) Tween-20, followed by a 1 h incubation with HRP-conjugated anti-mouse secondary antibody (R&D Systems) at 1:1.000 dilution at room temperature. Signal development was performed with Pierce ECL substrate solution, according to the manufacturer's instructions.

RNA extraction, cDNA preparation and real-time RT–PCR. RNA was extracted with the RNeasy Mini Kit (#74104, Qiagen). cDNA was generated with Superscript II Reverse Transcriptase (#18064-014, Invitrogen) and oligo-dT (#18418020, Invitrogen).

Evaluation of *p14^{ARF}* and *cyclin E* mRNA status was done by real-time PCR with reverse transcription[58] (RT–PCR) using the Platinum SYBR green qPCR SuperMix-UDG (#11733038, Invitrogen). Cyclers used were a DNA-Engine-Opticon (MJ-Research) and an ABI Prism 7300 (Applied Biosystems). Primers sequences for *p14^{ARF}*: first set: 5′-ATGGTGCGCAGGTTCTTGGTGA-3′; 5′-GGGGTCGGCGCAGTTGGGCTCA-3′, second set: 5′-CTACTGAGGAGCCAGCG-TCTA-3′; 5′-CTGCCCATCATCATGACCT-3′, cyclin E: 5′-GCGCAAAGGGGGAA-GGGGTA-3′; 5′-hemGCTCCTTCGCATCCCTGTGGA-3′, *GAPDH*: 5′-AGCCAC-ATCGCTCAGACAC-3′; 5′-GCCCAATACGACCAAATCC-3′, *PBGD*: 5′-TGCAA-CGGCGGAAGAAAACA-3′; 5′-GCAGATGGCTCCGATGGTG-3′, and *p19^{ARF}*: 5′-CGGAATCCTGGACCAGGTG-3′; 5′-ACCAGCGTGTCCAGGAAGC-3′. Rodent GAPDH was used as control (ABI). PCR reactions profiles were: an initial 10-min step at 95 °C, followed by 40 cycles of 95 °C for 25 s, 62 °C for 20 s and 70 °C for 20 s.

For RT–PCR analysis of the 47S pre-rRNA, nucleolar RNA was extracted from H1299 cells using TriReagent (Applied Biosystems). A total of 2 μg of RNA was reverse transcribed (Applied Biosystems). PCR was performed with Power SYBR Green (Applied Biosystems). Amplification was conducted with an initial 10-min step at 95 °C, followed by 40 cycles of 95 °C for 15 s and 60 °C for 1 min. The 47S pre-rRNA primers were 5′-CCTGCTGTTCTCTCGCGCGTCCGAA-3′ and 5′ AACGCCTGACACGCACGGCACGGA-3′. For internal control, the primers 5′-AAACGGCTACCACATCCA-3′ and 5′-CCTCCAATGGATCCTCGT-3′ for the 18S rRNA were used. Data were analysed using the comparative cycle threshold method with normalization of the raw data to the 18S rRNA. The results are presented as *n*-fold changes versus the values in untreated sample. The mean value was calculated from three independent measurements.

rRNA pulse-chase analysis. Pulse-chase for rRNA analysis was performed employing H1299 cells transfected with *ARF* siRNA. Twenty-four hours after transfection, ATM was inhibited by administration of Ku55933. The next day cells were starved of methionine for 15 min in 6-well plates with 2 ml of methionine-free medium. Subsequently, cells were labelled with 25 μCi ml^{-1} of L-[methyl-^{3}H]-methionine (#NET061X001MC, Perkin Elmer) for 30 min followed by incubation in medium containing cold methionine for indicated lengths of time. Finally, after washing with PBS, total RNA was extracted and purified with an RNA isolation kit (#74104, Qiagen). RNA quantification was performed by gel electrophoresis in a TBE 1.2% agarose gel with ethidium bromide. Equal amounts (10 μg) of RNA were loaded onto 1% agarose denaturing gel containing 0.55 M formaldehyde. The RNA was electrophoretically fractionated and transferred onto a Porablot N+ membrane (#741281, Macherey-Nagel). The membrane was dried and sprayed with EN3HANCE (#6NE970C, Perkin Elmer) and the film exposed for 10 days at −80 °C in the dark. Data were obtained from independent triplicates.

LC–MS analysis of NPM immunoprecipitation eluates. Trichloroacetic acid (TCA) precipitation was used for protein purification of the NPM/B23 immunoprecipitation eluates. TCA (10 M) was added to eluates at a volume ratio of 1:3 (TCA/sample), samples were kept at 4 °C for an hour and the precipitate was centrifuged at 16,000*g* for 10 min at 4 °C. Purified protein pellets were washed twice with ice-cold tetrahydrofuran (THF) and after THF removal they were dissolved in 0.5 M triethylammonium bicarbonate with 5 min heating at 90 °C and tip sonication. Proteins were reduced by addition of 50 mM tris-2-carboxymethyl phosphine (TCEP), followed by 1 h incubation at 60 °C. Cysteines were blocked by addition of 200 mM methyl methanethiosulphonate in isopropanol and 10 min incubation at room temperature. For trypsin digestion, 1 μl of trypsin (Roche) solution (500 ng μl^{-1}) was added into the protein sample and incubated for 12 h at 37 °C. The resultant peptides were dried with a SpeedVac concentrator and purified using C18 zip tips (Millipore). The equilibration, loading and washing buffer was 3% acetonitrile and 0.1% formic acid and the elution buffer was 80% acetonitrile and 0.1% formic acid. During all steps the working volume was 10 μl, which was slowly pumped 20 times during each step. The purified peptides were dried with a SpeedVac concentrator.

The LC–MS/MS experiments were performed on the hybrid quadrupole–time-of-flight QSTAR XL (AB Sciex) mass spectrometer retrofitted to a 1100 nano-HPLC system equipped with a micro well plate autosampler (Agilent Technologies). Each sample was reconstituted in 25 μl mobile phase A (2% ACN and 0.1% formic acid) and 4 μl of this solution was injected at 150 nl min^{-1} into a 0.075 × 200 mm reverse-phase capillary column (Zorbax C18, 300 Å pore, 3.5 μm particle) retrofitted onto the nanoelectrospray source and connected to a 1P-4P-coated, 15 μm tip ×360 μm outer diameter ×75 μm inner diameter PicoTip nanoelectrospray emitter (New Objective). Peptides were gradually eluted between 15 and 50% of mobile phase B (98% ACN and 0.1% formic acid) for a 120 min time period. During the 1 s + TOF MS survey scan of the information-dependent acquisition method, the top seven most abundant ions with a minimum ion signal of 30 cps and charge of + 2 to + 4 were selected for collision-induced dissociation fragmentation and acquisition of product ion spectra with 1 s accumulation time in enhance-all mode. Precursors were fragmented using rolling collision energy and were excluded from further targeting for 60 s after the acquisition of one spectrum. The *m/z* range for the MS experiments was 300–2,000 and for the MS/MS experiments was 80–2,000.

All tandem-MS spectra were subjected to ProteinPilot beta 4 (AB Sciex) software analyses for peptide and protein identification. The searching parameters against the Human SwissProt database included the phosphorylation emphasis option (see the Bioinformatic analysis section).

iTRAQ-based proteomic analysis. For the investigation of the global proteomic changes in the H1299 cell line associated with the various ATM kinase states, affecting ARF status, an iTRAQ-based proteomic approach was applied[40,41]. The H1299 cell pellets were dissolved in 200 μl triethylammonium bicarbonate (TEAB) buffer 0.5 M containing 0.05% sodium-dodecyl-sulphate (SDS) under vortex mixing, 5 min heating at 90 °C into a heating block and 20 s tip sonication with pulses. The protein content of cell lysates was measured with the Bradford method (Bio-Rad Protein Assay, Bio-Rad), using a calibrated spectrophotometer (Biomate, Thermo) with standard bovine serum albumin solutions according to the manufacturer's instructions. For each cell lysate 100 μg of total protein diluted in 20 μl TEAB 0.5 M and 0.05% SDS was prepared for reduction, cysteine blocking and trypsin digestion. Proteins were reduced by addition of 2 μl tris-2-carboxymethyl phosphine (TCEP) 50 mM followed by 60 min incubation at 60 °C. Cysteines were methylthiolated by addition of 1 μl 200 mM methyl-methanethiosulphonate in isopropanol and 10 min incubation at room temperature. For trypsin proteolysis, 6 μl trypsin (Roche) solution (500 ng μl^{-1}) and 11 μl ultrapure water were added into the protein mixtures (protein/trypsin 33:1, trypsin 75 ng μl^{-1}), which were then incubated for 12 h at 37 °C. For peptide iTRAQ labelling, 50 μl of isopropanol was added to each room-temperature iTRAQ-8plex reagent vial and then the content of one iTRAQ reagent vial was transferred to one sample tube for all of the samples (113:DMSO, 114:Ku55933 +control-siRNA, 115:*PP1* siRNA, 116:Ku55933 + *ARF* siRNA, 117:DMSO, 118:Ku55933 +control-siRNA, 119:*PP1* siRNA, 121:Ku55933 +*ARF* siRNA) (numbers denote the *m/z* of the iTRAQ reporter ions used for relative quantification, each corresponding to a different condition, for example, 113:DMSO, 114:(Ku55933+ control-siRNA) and so on, see figure legend 5c and end of section).

Thus, one iTRAQ 8-plex experiment, which contained 4 different conditions, was a duplicate run within the same experiment. The iTRAQ-labelled samples were mixed after 2 h of reaction at room temperature and the mixture was dried with a centrifugal vacuum concentrator (Eppendorf 5301). The advantage of this iTRAQ approach is that all samples were analysed simultaneously in duplicate and under the same experimental conditions. Therefore, the random analytical error was minimized, while deep proteome coverage was achieved[41].

The iTRAQ-labelled peptide mixture fractionation was performed with high-pH reverse-phase chemistry on a Dionex P680 HPLC pump equipped with a PDA-100 photodiode array-detector using a pC18 column (Waters, 150 × 4.6 mm, 7 μm). Mobile phase (A) was an aqueous buffer containing 30 mM ammonium formate at pH 10 adjusted by dropwise addition of ammonium hydroxide and mobile phase (B) was acetonitrile and 0.05% ammonium hydroxide. The dried peptide mixture was dissolved in 200 μl 95:5 A/B and centrifuged for 5 min at 16,000*g* The supernatant sample volume was injected through a 200 μl sample loop into the column with an isocratic composition of 5% B for 10 min followed by gradient elution of 1% B min^{-1} for 55 min at flow rate 1 ml min^{-1}. The fractions were collected with a time-dependent manner every 1 min starting from 10 min until the ultraviolet signal response at 215 nm returned to the baseline. Collected fractions were dried with a centrifugal vacuum concentrator and stored at −20 °C until the LC–MS/MS analysis.

All LC–MS/MS experiments were performed on the hybrid quadrupole–time-of-flight QSTAR XL (AB Sciex) mass spectrometer retrofitted to a 1100 nano-HPLC system equipped with a micro well plate autosampler (Agilent Technologies). Each peptide fraction was reconstituted in 25 μl mobile phase A (2% ACN and 0.1% formic acid) and 4 μl of this solution was injected at 150 nl min^{-1} into a 0.075 × 200 mm reverse-phase capillary column (Zorbax C18, 300 Å pore, 3.5 μm particle) retrofitted onto the nanoelectrospray source and connected to a 1P-4P-coated, 15 μm tip × 360 μm outer diameter ×75 μm inner diameter PicoTip nanoelectrospray emitter (New Objective). Peptides were gradually eluted between 15 and 50% of mobile phase B (98% ACN and 0.1% formic acid) for a time period of 120 min. During the 1 s + TOF MS survey scan of the information-dependent acquisition method, the top seven most abundant ions with a minimum ion signal of 30 cps and a charge + 2 to + 4 were selected for collision-induced dissociation fragmentation and acquisition of product ion spectra with 1 s accumulation time in enhance-all mode, using the advanced settings of 'exclude isotopes' and 'use pattern'. Precursors were fragmented using rolling collision energy and excluded from further targeting for 100 s after acquisition of one spectrum. The *m/z* range for the MS experiments was 300–2,000, and for the MS/MS experiments was 80–2,000.

Tandem MS spectra were subjected to ProteinPilot beta 4 (AB Sciex) software analyses for protein identification and quantification. Searching parameters against the Human SwissProt database included false discovery rate analysis, bias correction and background correction of the iTRAQ ratios (see the Bioinformatic analysis section).

ChIP assay. ChIP assay was performed as previously described[59]. A 242-base-pair (bp) fragment in the cyclin E promoter was amplified with the following primers 5′-GCGCAAAGGGGGAAGGGGTA-3′ and 5′-GCTCCTTCGCATCCCTGTGGA-3′[43]. As a negative control, a 104-bp amplicon, located > 1,500 bp from the transcription start site (Fig. 6d), was amplified with the following primers 5′-CAGCCTGAGCAACATAGCAA-3′ and 5′-TCCACAGCTCCTCTGTCCTT-3′ (ref. 43). As inputs we used products that corresponded to PCR reactions containing 1% of the total chromatin extract used in the immunoprecipitation reactions. PCR amplifications were performed as previously described[43].

Growth curve analysis. Growth curve analysis was performed four times, as previously described[58,59].

DOI: 10.1038/ncb2795

Soft agar assay. Soft agar assay was performed as previously described[59]. Experiments were performed in four independent replicates.

Lentivirus production—titration and transduction of H1299-xenograft tumours. For the production of lentiviral particles, 5×10^6 HEK293T cells were seeded in 10 cm plates and transfected with 15 μg expression vector and third-generation packaging plasmids (15 μg pMDLg/pRRE, 6 μg pRSV-REV, 3 μg pMD2.G) using 50 μl Lipofectamine 2000 transfection reagent (Invitrogen). For the silencing of ATM in xenograft tumours from H1299 and H1299-*ARF* shRNA cells, 3 different pLKO.1-short hairpin RNA MISSION vectors (Sigma; Supplementary Table S4) were employed. The pLKO.1 TurboGFP (Sigma) was used as a control vector. Viral supernatants were collected 48, 72 and 96 h post-transfection and concentrated using the LentiX concentrator (Clontech) according to the manufacturer's instructions. Viral RNA was isolated from 150 μl of each concentrated lentivirus using the Viral RNA isolation kit (Macherey-Nagel) and titration was done by the LentiX qRT–PCR Titration Kit (Clontech) according to the manufacturer's instructions. Lentivirus transduction by intratumoral injections of GFP, *GFP* siRNA (non-target-shRNA) or shATM lentiviral particles (with a viral titre of 6.2×10^{11} ml^{-1} lentiviral particles per injection) took place daily for a period of five days and every 2 days for another three weeks after the appearance of tumours.

Xenografts, animals and human samples. H1299 ctl-shRNA cells (10^6 cells in 200 μl of PBS) were subcutaneously injected into each flank of a group ($n = 5$) of randomly selected 8–12-week-old SCID (*Mus musculus*) mice. In a second group of 5 mice, 10^6 H1299 ctl-shRNA or *ARF* shRNA cells were subcutaneously injected into both flanks of each mouse. Two weeks later macroscopically visible tumours had developed. Subsequently, lenti-non-target-shRNA or lenti-*ATM* shRNA was injected respectively according to the timetable presented in Supplementary Fig. S8d. In another type of experiment, mice randomly assigned into three groups of 4 animals were examined. The first and second groups were injected with H1299 ctl shRNA, and the third one was injected with cells carrying *ARF* shRNA. After tumour visualization, the first group was injected with lenti-non-target-shRNA, whereas the second and third with lenti-*ATM* shRNA. At the end of the four-week treatment the animals (Supplementary Fig. S8a) were euthanized, and the tumours were excised, weighed, formalin fixed and processed for paraffin embedding, as previously described[59].

Male, 8–12-week-old NOD/SCID mice randomly assigned into 2 groups of 3 animals, were generally employed. Whole body irradiation treatment was performed by applying 2 Gy per day (for a total of 3 days) employing a ^{60}Co source and tissue collection done after 4 days. In all animal experiments, no statistical method was used to predetermine sample size.

Formalin-fixed, paraffin-embedded specimens of 158 non-small cell lung carcinomas along with adjacent normal tissue, previously employed and molecularly characterized in other publications, were used in the present work[45,46,58,64,65]. All specimens were selected after local ethical committee approvals. None of the patients had undergone any cancer therapy before surgical resection of the lesions.

Immunohistochemistry analysis. Immunohistochemistry analysis was performed on formalin-fixed paraffin embedded samples as previously described[58,59]. Immunohistochemical stainings were evaluated independently by two experienced pathologists who were blinded to the data. A minimum of 10 independent optical fields per sample were counted and each IHC/sample was repeated minimum 3 times. Cutoff values were used to establish dichotomous variables as previously described (Supplementary Fig. S7a). Specifically, tumours with 10% staining percentage of cells or higher, were considered positive for ATM (ref. 66). For Chk2 expression the cutoff value was set to 60% (ref. 67). p16^{INK4A} staining was considered negative if there was no nuclear staining in cancer cells or there was weak focal staining. Cases with stained nuclei in all interpretable areas of the neoplasm were considered positive[68]. Similarly, p14^{ARF} expression was scored as negative in cases with no staining or weak focal staining (< 10% of cancer cells). Cases with stained cells in all interpretable areas of the neoplasm accounting for more than 10% of the total cancer cells were considered as positive[69]. Mean expression of p14^{ARF} was 53% (s.d. = 23%) for positive patients and 5% (s.d. = 4%) for negative patients.

Bioinformatic–biostatistical analysis. For protein identification and quantification, all proteomic raw data were converted to PRIDE XML format and deposited into the PRIDE database (http://www.ebi.ac.uk/pride/; Supplementary Table S7; username: review39906 and password: ym ~8h5bZ). All tandem-MS spectra were subjected to ProteinPilot v 4.0 (AB Sciex) software for protein identification and quantification, and mass spectra were searched against the Human SwissProt database, using the in-built Paragon algorithm[70]. The false discovery rate was controlled at 1% (ref. 71). Bias and background correction was applied to the iTRAQ levels. The protein-level iTRAQ ratios were then calculated. All aforementioned analysis was also carried out in Protein Pilot.

For iTRAQ ratio meta-analysis, iTRAQ ratios were exported from Protein Pilot, and were consequently $\log_2$ transformed, centred and the respective technical duplicates averaged. Proteins whose $\log_2$ ratio standard deviation exceeded their respective average $\log_2$ ratio absolute value (indicating a non-consistent measurement) were filtered out from the protein list. The above procedures were carried out in R language[72].

For pathway analysis, proteins from the previous procedure were imported into Ariadne Pathway Studio v 9.0 and analysed for biological context against Ariadne's canonical cell-process pathways using the in-built gene set enrichment analysis procedure[73,74].

For statistical analysis of proteomic data, heat map visualizations, performing protein-level hierarchical clustering based on the protein $\log_2$ ratio Euclidean distance of specific protein groups across various states, were created using the R-package g-plots[75]. Fisher's exact test was used for calculating enrichment scores for specific protein groups. The confidence level was set to 95%; hence P values < 0.05 were considered significant.

For other biological explorations, analysis of variance, regression or t-test analyses were employed using the SPSS v17.0 software. All data to be analysed were first checked for compliance to assumptions of the employed tests and similar variance.

56. Mitsuhashi, S. *et al.* Tautomycetin is a novel and specific inhibitor of serine/threonine protein phosphatase type 1, PP1. *Biochem. Biophys. Res. Commun.* **287,** 328–331 (2001).
57. Gorgoulis, V. G. *et al.* p53 activates ICAM-1 (CD54) expression in an NF-kB-independent manner. *EMBO J.* **22,** 1567–1578 (2003).
58. Liontos, M. *et al.* Deregulated overexpression of hCdt1 and hCdc6 promotes malignant behavior. *Cancer Res.* **67,** 10899–10909 (2007).
59. Sideridou, M. *et al.* Cdc6 expression represses E-cadherin transcription and activates adjacent replication origins. *J Cell Biol.* **195,** 1123–1140 (2011).
60. Bartkova, J. *et al.* Oncogene-induced senescence is part of the tumorigenesis barrier imposed by DNA damage checkpoints. *Nature* **444,** 633–637 (2006).
61. Hershko, T. & Ginsberg, D. Up-regulation of Bcl-2 homology 3 (BH3)-only proteins by E2F1 mediates apoptosis. *J. Biol. Chem.* **279,** 8627–8634 (2004).
62. Cescutti, R., Negrini, S., Kohzaki, M. & Halazonetis, T. D. TopBP1 functions with 53BP1 in the G1 DNA damage checkpoint. *EMBO J.* **29,** 3723–3732 (2010).
63. Andersen, J. S. *et al.* Directed proteomic analysis of the human nucleolus. *Curr. Biol* **12,** 1–11 (2002).
64. Karakaidos, P. *et al.* Overexpression of the replication licensing regulators hCdt1 and hCdc6 characterizes a subset of non-small-cell lung carcinomas: synergistic effect with mutant p53 on tumor growth and chromosomal instability–evidence of E2F-1 transcriptional control over hCdt1. *Am. J. Pathol.* **165,** 1351–1365 (2004).
65. Zacharatos, P. *et al.* Distinct expression patterns of the transcription factor E2F-1 in relation to tumour growth parameters in common human carcinomas. *J. Pathol.* **203,** 744–753 (2004).
66. Honrado, E. *et al.* Immunohistochemical expression of DNA repair proteins in familial breast cancer differentiate BRCA2-associated tumors. *J. Clin. Oncol.* **23,** 7503–7511 (2005).
67. Kilpivaara, O. *et al.* Correlation of CHEK2 protein expression and c.1100delC mutation status with tumor characteristics among unselected breast cancer patients. *Int. J. Cancer* **113,** 575–580 (2005).
68. Geradts, J., Kratzke, R. A., Niehans, G. A. & Lincoln, C. E. Immunohistochemical detection of the cyclin-dependent kinase inhibitor 2/multiple tumor suppressor gene 1 (CDKN2/MTS1) product p16INK4A in archival human solid tumors: correlation with retinoblastoma protein expression. *Cancer Res.* **55,** 6006–6011 (1995).
69. Vestey, S. B. *et al.* p14ARF expression in invasive breast cancers and ductal carcinoma *in situ*–relationships to p53 and Hdm2. *Breast Cancer Res* **6,** R571–R585 (2004).
70. Shilov, I. V. *et al.* The Paragon Algorithm, a next generation search engine that uses sequence temperature values and feature probabilities to identify peptides from tandem mass spectra. *Mol. Cell Proteom.* **6,** 1638–1655 (2007).
71. Tang, W. H., Shilov, I. V. & Seymour, S. L. Nonlinear fitting method for determining local false discovery rates from decoy database searches. *J. Proteome Res.* **7,** 3661–3667 (2008).
72. R Development Core Team. R: a Language and Environment for Statistical Computing. R Foundation for Statistical Computing, Vienna, Austria. 409 (2012).
73. Subramanian, A. *et al.* Gene set enrichment analysis: A knowledge-based approach for interpreting genome-wide expression profiles. *Proc. Natl Acad. Sci. USA* **102,** 15545–15550 (2005).
74. Mootha, V. K. *et al.* PGC-1alpha-responsive genes involved in oxidative phosphorylation are coordinately downregulated in human diabetes. *Nat. Genet.* **34,** 267–273 (2003).
75. Warnes, G. R. Includes R source code and/or documentation contributed by (in alphabetical order): Bolker, B. et al. gplots: various R programming tools for plotting data. R package version 2.10.1 (2011).
76. Brooks, D. G., James, R. M, Patek, C. E., Williamson, J. & Arends, M. J. Mutant K-ras enhances apoptosis in embryonic stem cells in combination with DNA damage and is associated with increased levels of p19(ARF). *Oncogene* **20,** 2144–2152 (2001).

DOI: 10.1038/ncb2795

nature cell biology

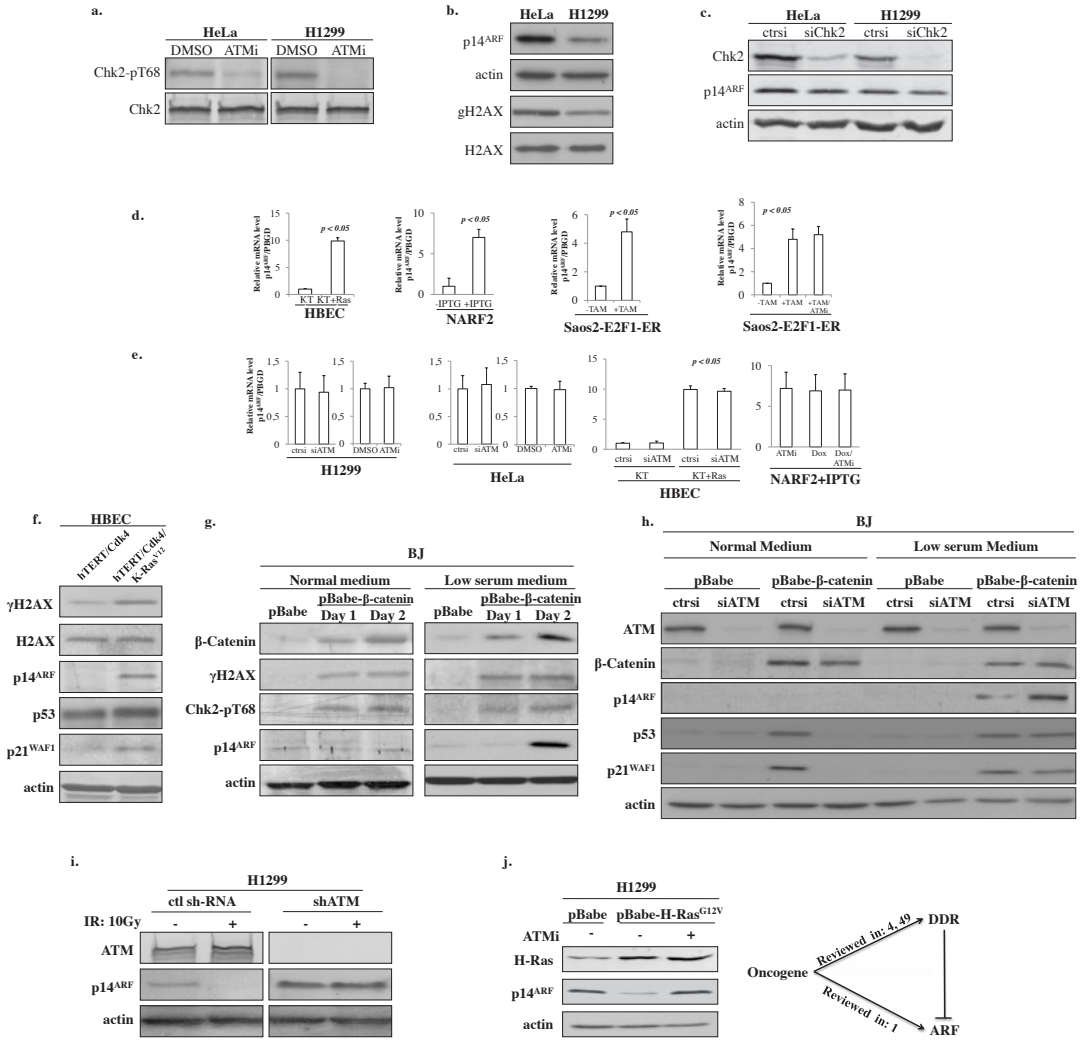

Figure S1 HeLa and H1299 cells exhibit signs of DDR activation and detectable levels of ARF expression, but Chk2 silencing does not affect $p14^{ARF}$ protein levels. **a.** Immunoblot (IB) analysis shows decreased phospho-Chk2 levels upon ATM inhibition (ATMi) in H1299 and HeLa cells, demonstrating the effectiveness of the inhibitor **b.** IBs depicting signs of DDR activity, assessed by gH2AX (see also **Figure 1a**), and detectable levels of $p14^{ARF}$ expression in HeLa and H1299 cells. **c.** IBs demonstrating that Chk2 silencing in HeLa and H1299 cells has no effect on $p14^{ARF}$ levels. $p14^{ARF}$ mRNA levels are induced by oncogenic stimuli (Cdk4, Ras and E2F1), but are unaltered after inhibition or silencing of ATM. Bars represent quantification of $p14^{ARF}$ mRNA levels as assessed by semi-quantitative real time RT-PCR in: **(d)** Human Bronchial Epithelial Cells (HBECS) (KT: hTERT, Cdk4 and KT transfected with activated K-Ras^{V12}), NARF cells (with or without IPTG induction) and Saos2-E2F1-ER (non-induced, TAM-induced and TAM-induced + ATMi), and in: **(e)** H1299, HeLa, HBECs cells transfected with control siRNA, si*ATM,* DMSO (control) and Ku55933 (ATMi), induced NARF2 treated with Doxorubicin and Doxorubicin+Ku55933, respectively. ($p < 0.005$, t-test, error bars indicate SDs, n=4 real time RT-PCR runs). Silencing of ***ATM*** enhances oncogene-induced $p14^{ARF}$ expression in BJ cells and HBECs**. f.** IB analysis complementing **Figure 1c** results showing the status of DDR activation and $p14^{ARF}$ levels in immortalized HBECs (hTERT, Cdk4) and immortalized HBECs with K-Ras^{V12}. Genetically manipulated HBECs expressing various oncogenes[17,16,76] were employed as normal cells do not demonstrate signs of DDR activation[46] and ARF levels are negligible[1]. **g.** IB analysis results showing that β-catenin transfected diploid BJ human fibroblasts exhibit DDR activation, while upregulation of $p14^{ARF}$ levels require additionally low serum conditions, as previously reported[20]. **h.** IB analyses, complementing panel **g**, demonstrating that the increased $p14^{ARF}$ protein levels in BJ primary human fibroblasts due to β-catenin transfection and serum depletion was further enhanced after silencing of ATM. ATM regulates $p14^{ARF}$ protein stability. **i.** Silencing of ATM (shATM H1299 cells) protects ARF from DNA damage mediated downregulation. Oncogenic stimuli compete with active ATM in regulating ARF expression. **j.** IB analysis of $p14^{ARF}$ in H1299 cells infected with pBabe (control) or pBabe-Ha-Ras^{V12} and in the presence or absence of ATM inhibitor Ku55933, showing that the oncogenic challenge of H1299 cell (that already harbour mutant and activated K-Ras) decreases the endogenous levels of ARF that were re-established when ATM was inhibited. Apparently, the oncogene-ARF pathway, in this setting, has reached an activation plateau and any additional oncogenic stimulus activates ATM leading to ARF suppression **b.** Two signalling routes lead to ARF induction, oncogenic challenge[1] and ATM suppression. Given that oncogenes activate ATM, as well[4,7,46,49,60], oncogenic insults trigger two pathways with opposing effects on ARF expression. The outcome of this antagonism will depend on whether the rate of ARF production by oncogenes exceeds or not the rate of ARF destruction by the oncogene induced ATM pathway. Actin serves as loading control. ATMi= Ku55933 addition, PBGD= Porphobilinogen deaminase (house-keeping gene), Dox= Doxorubicin, ATMi= Ku55933 addition, ctrsi= control siRNA, TAM= 4-OH-Tamoxifen.

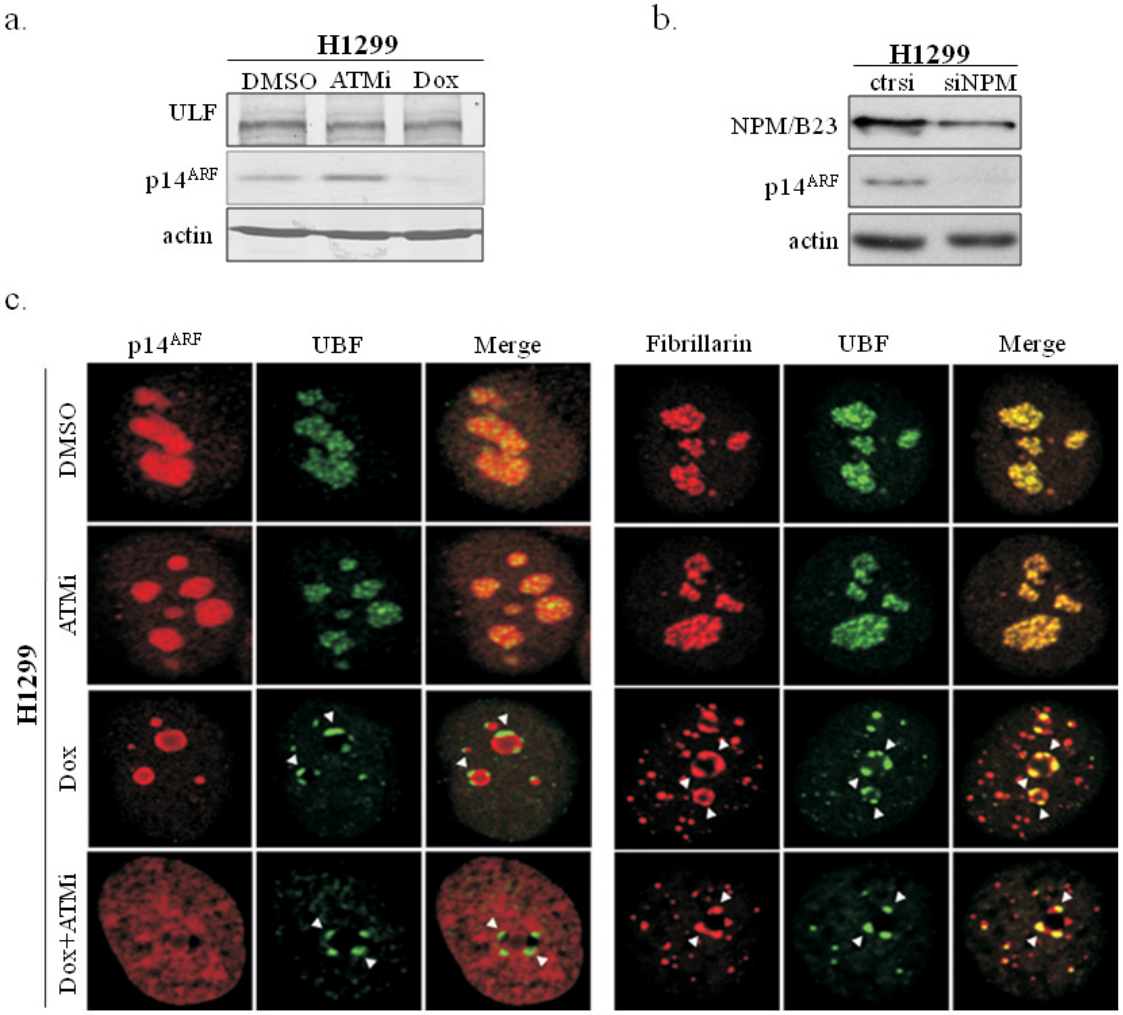

Figure S2 Activation of ATM promotes the degradation of ARF by disrupting the ARF-NPM/B23 complex. **a.** TRIP12/ULF protein levels remain unchanged after ATMi or Doxorubicin treatment in H1299 cells. Actin serves as loading control. ATMi= Ku55933 addition. **b.** IB analysis in siNPM/B23 H1299 cells showing downregulation of $p14^{ARF}$ denoting the significance of NPM/B23 in $p14^{ARF}$ stabilization. **c.** Nucleolar changes after exposure to ATM inhibition and Doxorubicine. H1299 cells were treated with doxorubicine (2uM) and the ATM inhibitor Ku55933 (10uM) for 24h. Untreated and treated cells were fixed and subjected to immunofluorescence staining with antibodies against the indicated nucleolar markers. Fibrillarin and UBF nucleolar cap structures are indicated by *arrowheads*. Fluorescence signals were analyzed by CLSM. Dox= Doxorubicin, ATMi= Ku55933 addition.

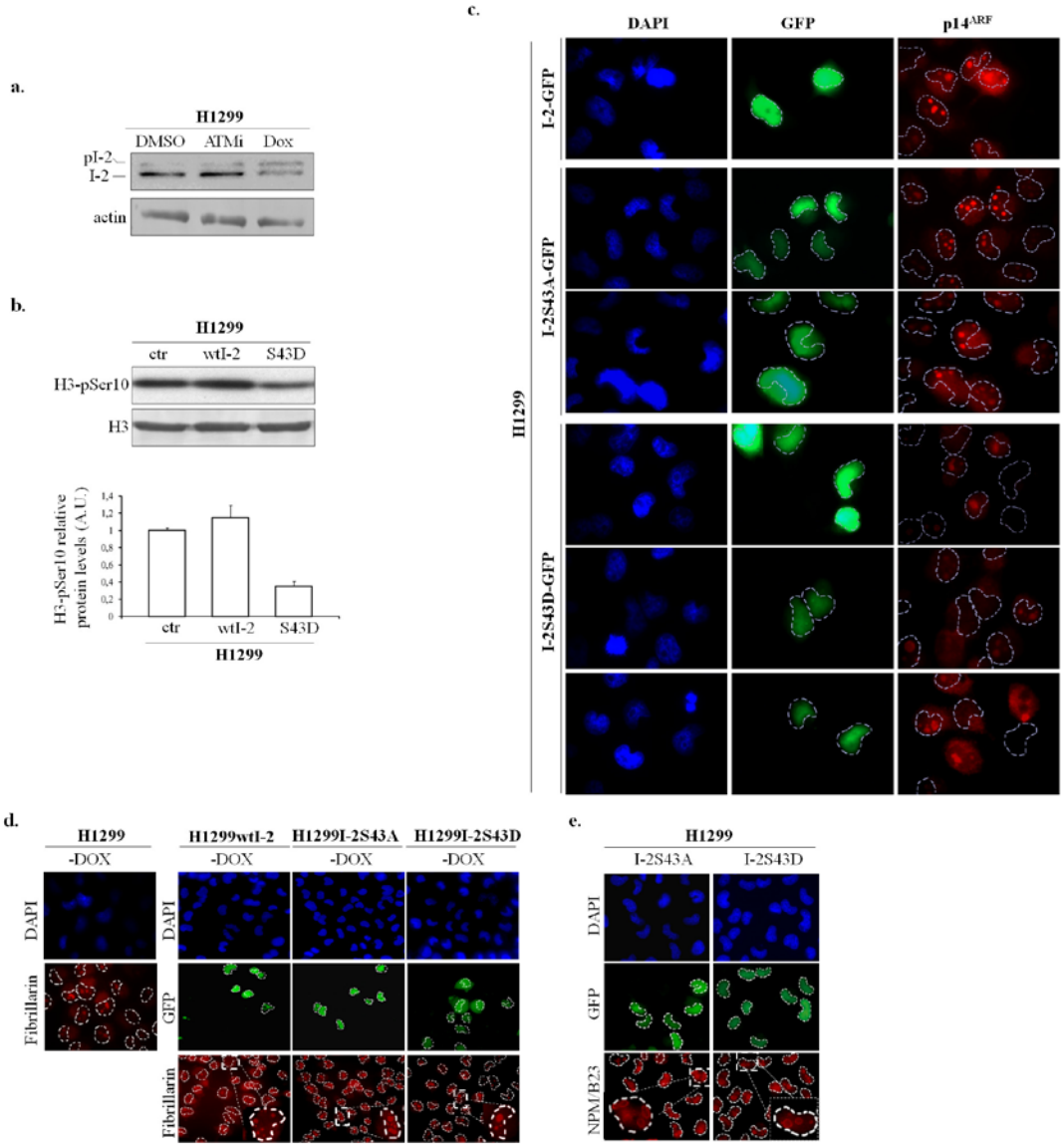

Figure S3 ATM regulates PP1 activity through I-2. **a.** IB analysis of I-2 in H1299 cells treated with DMSO, Ku55933 or Doxorubicin. pI-2 designates the slower migrating phosphorylated form of I-2. **b.** The phosphomimetic S43D mutation of I-2 abrogates its inhibitory effect over PP1. Immunoblot analysis for H3Ser10 in H1299 cells transfected with empty vector, wtI-2 or I-2S43D, which served as a positive control of increased PP1 activity. Histogram depicting quantification of H3Ser10 protein levels in H1299 cells transfected with the phosphomimetic S43D (p = NS and $p < 0.001$ (S43D) respectively, t-test, error bars indicate SDs, n=3 blots). **c.** Immunofluorescence analysis demonstrating absence of $p14^{ARF}$ staining in nuclei transfected with the phosphomimetic I-2S44D-GFP compared to I-2-GFP and I-2S44A-GFP mutant form in H1299 cells. Overexpression of wtI-2 or I-2S43A and I-2S43D mutants does not affect nucleolar integrity or NPM/B23 localization, as shown by immunofluorescence analysis for the nucleolar marker fibrillarin **(d)** and NPM/B23 **(e)**. The efficiency of the transfection was examined with GFP. Nuclei were stained with DAPI. The efficiency of the transfection was examined with GFP. Dotted lines define nuclei. Actin and H3 serve as loading control. NS=non-significant, Dox= Doxorubicin, ATMi= Ku55933 addition, A.U.=arbitrary optical density units

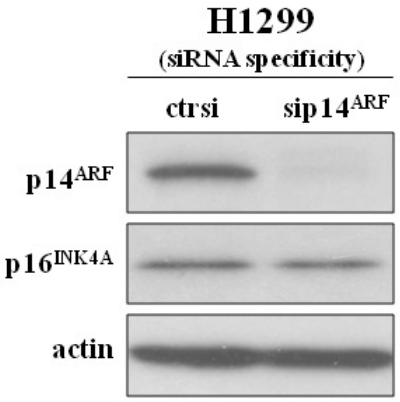

Figure S4 Representative immunoblot showing the specificity of the sip14^{ARF} as it does not affect p16^{INK4A} expression.

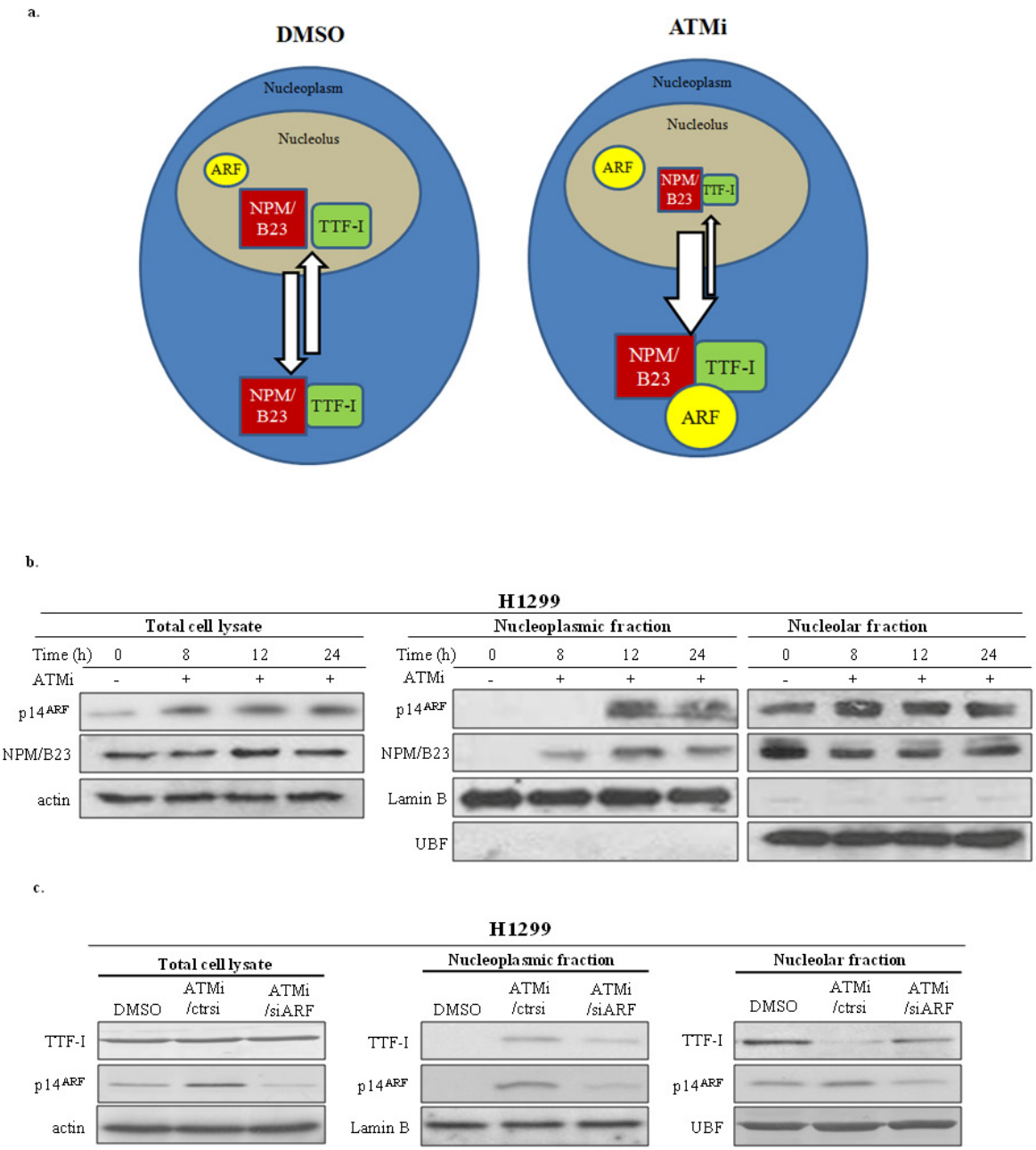

Figure S5 ATM-dependent p14^{ARF} regulation affects ribosomal biogenesis. **a.** Schematic presentation of the findings described in panels **b** and **c**. **b.** IBs depicting the localization over time of NPM/B23 and p14^{ARF} in ATM compromised H1299 cells in total lysates, nucleoplasmic and nucleolar fractions. **c.** Modulation of p14^{ARF} levels by ATMi affects TTF-I nucleoplasmic/nucleolar localization. IBs depicting the status of TTF-I and p14^{ARF} in H1299 total cell lysates, nucleoplasmic and nucleolar fractions, respectively upon DMSO, ATMi and ATMi/siARF treatments.

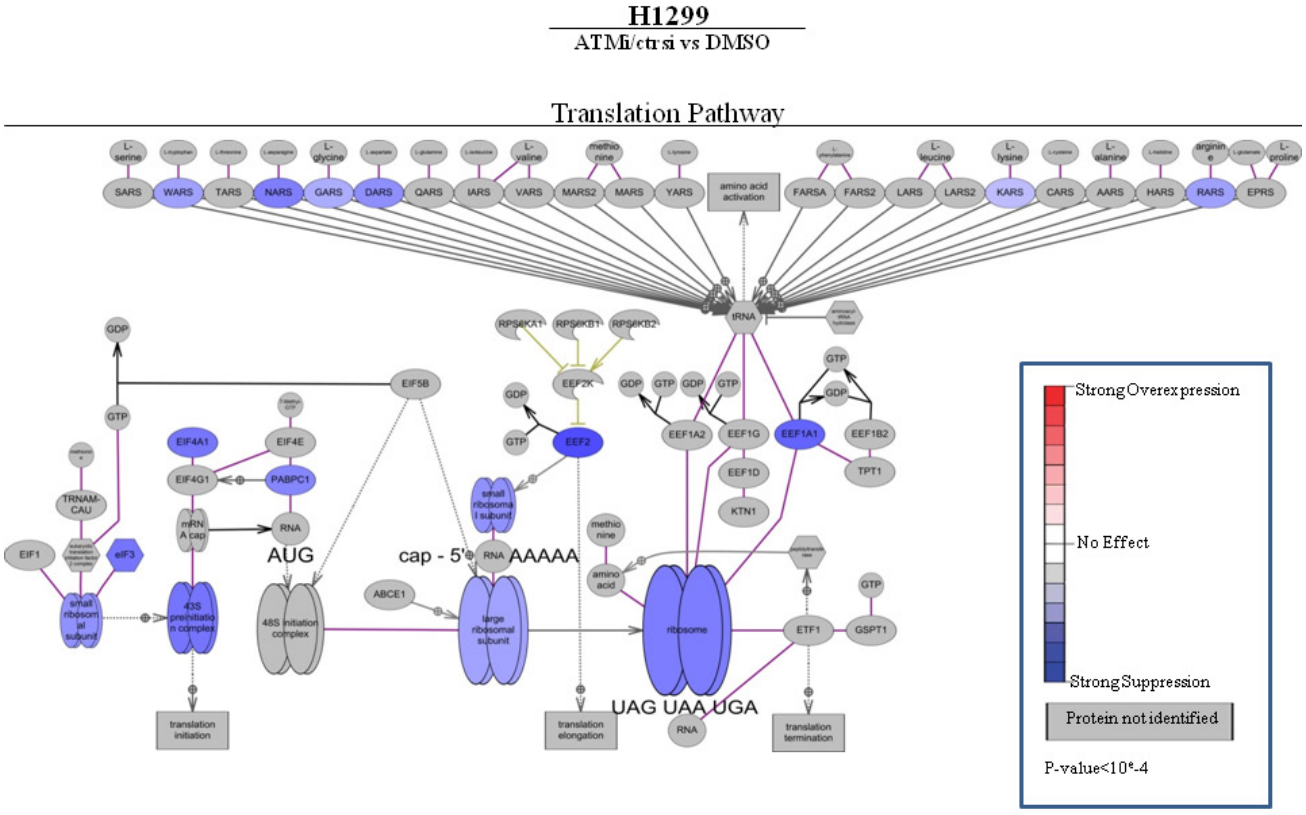

Figure S6 Gene Set enrichment analyses revealed the depicted "translation pathway" to be among the most significantly affected ones ($p < 10^{-4}$) by ATM inhibition (ATMi). ATMi= Ku55933 addition

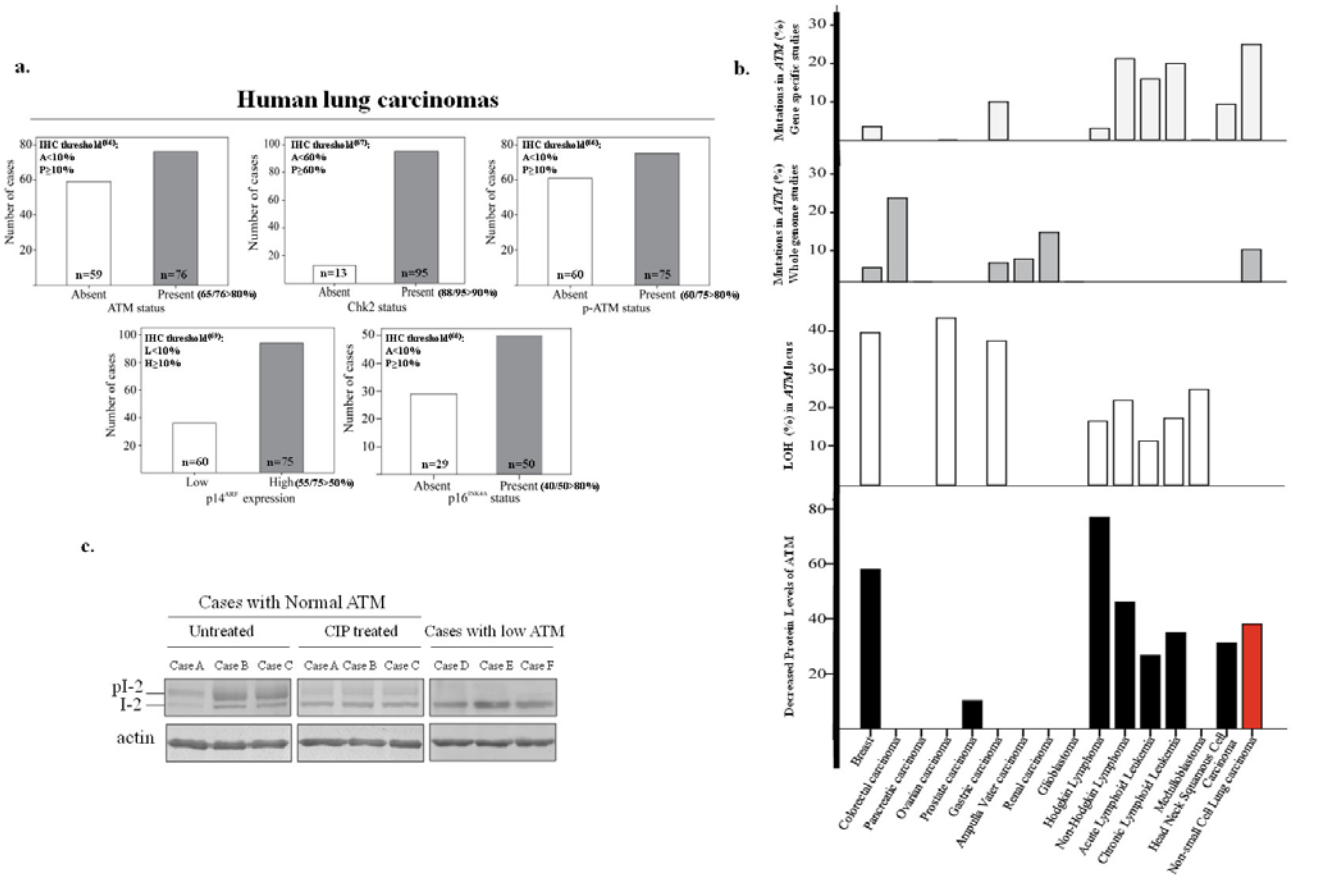

Figure S7 ATM abrogation is inversely related with ARF expression in human cancer. **a.** Cumulative data (histograms) depicting the distribution of the lung cancer cases examined in the current work, according to the status of ATM, p-ATM, Chk2, $p14^{ARF}$ and $p16^{INK4A}$ [66-69]. **b.** Meta-analysis regarding alterations in the *ATM* gene and its protein product levels. Histograms represent the percentage of ATM alterations in the corresponding neoplasias. The red bar is the result of the current study. **d.** Phosphorylated I-2 PP1 regulatory subunit expression corroborates with ATM status in human lung carcinomas. Cases with normal ATM demonstrate by IB analysis increased expression of the phosphorylated I-2 PP1 regulatory subunit (pI-2). The reduced intensity of the slower migrating pI-2 band upon calf intestinal phosphatase (CIP) treatment of the blots denotes the specificity of the antibody used for the detection of the phosphorylated form of the I-2 subunit. In contrast, cases with low ATM levels do not show any levels of the pI-2 subunit. [14,30,33] Actin serves as loading control.

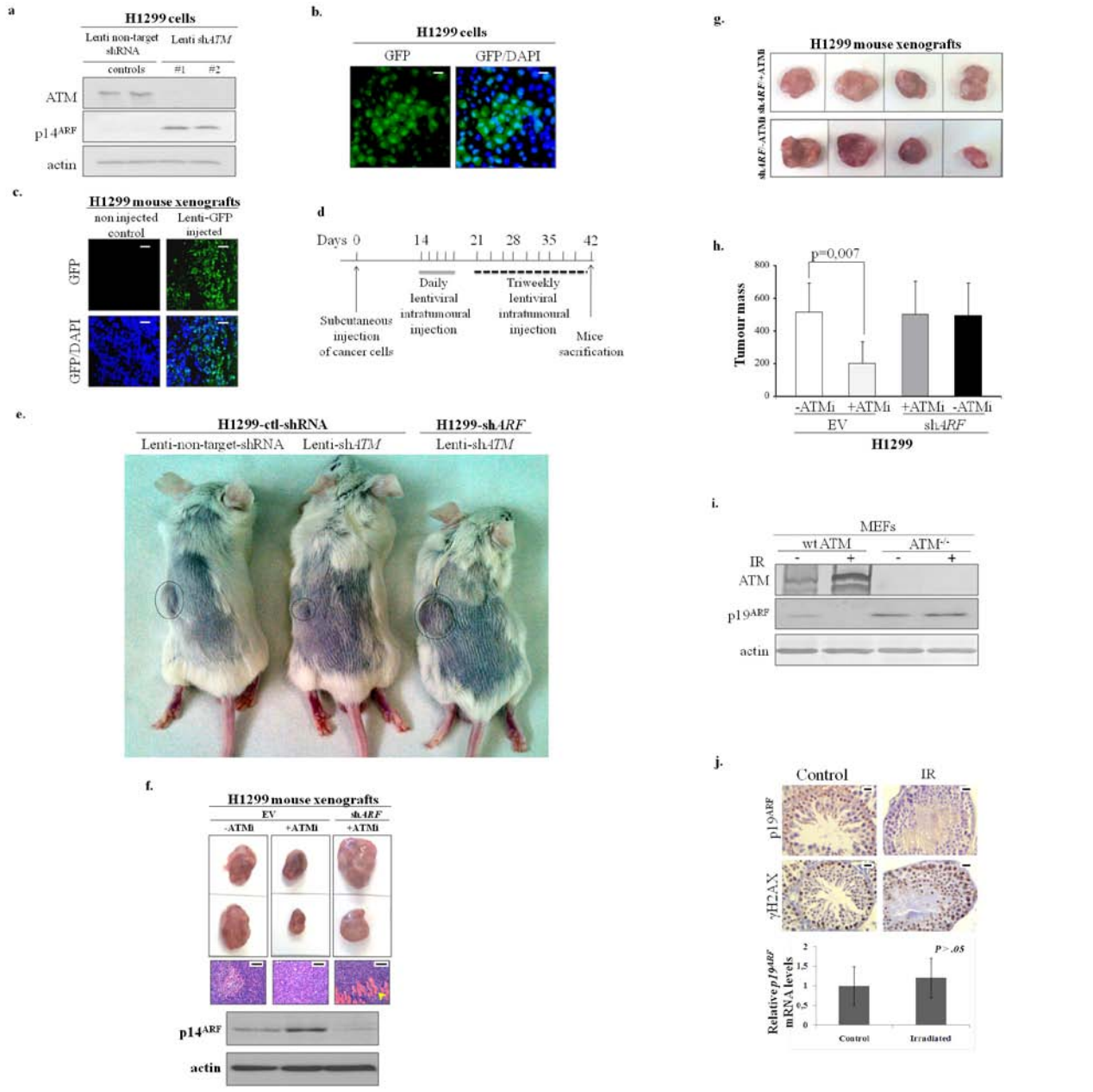

Figure S8 ATM abrogation is inversely related with ARF expression in tumours generated from grafted H1299 cells in immuno-compromised mice. **a.** Validation of lenti-shATM silencing sequences **(see Suppl. Table 4)** in H1299 cells showing down-regulation of ATM followed by increased expression of ARF. Actin serves as loading control. **b.** Successful transduction of H1299 cells with lenti-GFP. Scale bar: 25μm. **c.** Successful delivery and expression of GFP after injecting H1299-mock xenografts with lenti-GFP. Nuclei were stained with DAPI. Scale bar: 50μm. **d.** Timetable of injections containing either pLKO.1 lenti-shATM or pLKO.1 lenti-non-target shRNA to H1299-mock and H1299-shARF xenografts. **e.** Tumours generated from grafted H1299 cells in immuno-compromised mice exhibited significantly reduced size after suppressing ATM expression for a period of 4 weeks **(see also panels f-h)** by injecting the tumours with lenti-shATM. The tumours remained unaffected when shATM was administrated in H1299-shARF xenografts. **f.** Tumours generated from grafted H1299 cells in immuno-compromised mice exhibited significantly reduced size after inhibition of ATM activity (ATMi), but remained unaffected in size when ATM inhibitor (ATMi) was administrated in H1299-shARF xenografts. Hematoxylin-eosin sections from the developed tumours (yellow arrow depicts invasion of abdominal wall muscle layer). Scale bar: 200μm**.** IB analysis depicting the p14ARF protein levels in the control (EV), ATMi/EV and ATMi/shARF tumours. **g.** There was no significant difference in mass between tumours developed from H1299-shARF injected cells, with or without ATMi administration. **h.** Histogram presents the average mass between the groups of generated tumours ($p = 0.007$ and $p =$ NS respectively, t-test, error bars indicate SDs, from 3 groups of 4 animals/group). Dependence of ARF expression upon ATM status in MEFs and mouse testis. **i.** IBs showing that ATM null mouse embryo fibroblasts (MEFs) demonstrate higher levels of ARF compared to $ATM^{+/+}$ MEFs, which remain unaffected upon irradiation, while in irradiated $ATM^{+/+}$ MEFs ARF expression is lost. **j.** IHC staining demonstrating loss of ARF expression in mouse seminiferous tubules after irradiation (Scale bar: 50μm). Histogram depicts $p19^{ARF}$ mRNA levels in mouse testis before and after irradiation ($p =$ NS, t-test, error bars indicate SDs, from 3 animals/group). EV=empty vector, ATMi=caffeine addition, IR=irradiation, NS=non-significant.

Figure S9 Full scans of blots.

Supplementary Table Legends

Supplementary Table 1 Analytical presentation of all peptides and their modification recognized by the LC-MS/MS analysis from NPM-immunoprecipitated H1299. (see full table organized in accompanying excel file)

Supplementary Table 2 Peptides (**a**), proteins (**b**) and filtered proteins (**c**) presenting high degree of reproducibility. Section (**c**) also contains p-values indicative of differential expression with confidence being set to 95%. (see full table organized in accompanying excel file)

Supplementary Table 3 Studies examining genetic and epigenetic alterations in *ATM* and its mRNA and protein expression status in several sporadic malignancies

Supplementary Table 4 Lentiviral vectors (MISSION®) and inserts used from Sigma-Aldrich.

Supplemental Table 5 List of antibodies employed in immunohistochemistry, immunofluorescence, immunoblotting, immunoprecipitation and chromatin immunoprecipitation analyses.

Supplementary Table 6 Primers for mutagenesis and sequencing.

Supplementary Table 7 Datasets accession numbers for proteomic results deposited in PRIDE.

Note on Supplementary Table 1 and Supplementary Table 2:

Protein Pilot results are presented in **Suppl. Tables 1** and **2**. A description of the fields of the **Supplementary Tables 1** and **2** is the following:

Spectrum: Unique spectrum identifier (used within ProteinPilot)

Time: The LC-MS/MS run time in minutes when the peptide was detected

Prec m/z: Precursor mass over charge ratio

Prec z: Precursor charge

Prec MW: Precursor Molecular Weight (as calculated from Precursor mass over charge ratio)

Prot N or N : ProteinPilot unique protein identifier (used within ProteinPilot)

Best Sequence: Sequence of the peptide identified with the highest confidence

Modifications: Amino acid features/modifications with peptide residue number indicated

Conf: Peptide Confidence from ProteinPilot scoring algorithm

Theor MW: Theoretical Precursor Molecular Weight (Molecular Weight of the matched peptide)

z: Charge as calculated from the theoretical molecular weight

Contrib: Contribution value = –log-10 * [1 – (conf/100)]

Unused: Unused Protein score = $\sum$ peptide contribution values of unused peptides where, unused peptides = peptides not claimed by another protein. Scores greater than or equal to 0.88 provide an overall protein identification false discovery rate (FDR) < 1%.

Total: Total Protein score = $\sum$ peptide contribution values of total peptides where, total peptides = total peptides claimed by the specific protein

% Cov: Percentage of the total protein sequence covered with identified peptides

Accession #: Protein Accession Name

Name: Protein Name

Species: Species where the identified protein originates from

Peptides(95%): No of peptides claimed by the specific protein with Peptide confidence value > 95%

Δmass: Difference between Theoretical and Precursor Molecular Weights

Cleavages: Missed or non-specific cleavages report

Supplementary Table 3 legend

Studies examining genetic and epigenetic alterations in *ATM* and its mRNA and protein expression status in several sporadic malignancies

Abbreviations and Notes: Mutation analysis[a]: germ line mutations were excluded; LOH: loss of heterozygosity; Protein status[b]: protein levels were examined with Western blot (WB) analysis. In the studies where the protein levels were examined with a different method from WB, the method is mentioned separately; HNSCC: head and neck squamous cell carcinoma; NSCLC: non-small cell lung carcinoma; HL: Hodgkin lymphoma; NHL: non-Hodgkin lymphoma; ALL: acute lymphocytic/lymphoblastic leukemia; CLL: chronic lymphoblastic leukemia; VC: ampulla Vater carcinoma; I/N/D: increased/normal/decreased levels in the tumour versus normal sections; NE: not examined; E: examined; n: number of cases examined; MSP: methylation-specific polymerase chain reaction; IHC: immunohistochemistry; 0/74[1]: none of the specimens analyzed exhibited hypermethylation of *ATM* promoter as assessed by MSP analysis; D:70/92[1]: IHC analysis of ATM protein status showed that 70 cases exhibited low ATM score in the cancerous region (IHC score is assigned as the product of intensity of nuclear immunoreactivity and the percentage of tumour cells with positive immunostaining) in comparison with the normal counterpart; D(n=28)[2]: median (25^{th} percentile, 75^{th} percentile) mRNA levels in cancerous (C) region versus adjacent normal tissue (N), N: 5.6 (3.9, 8.3) versus C: 2.9 (1.8, 5.3) ($p<0.001$) (a number of patients had received neoadjuvant chemotherapy); 18/23[3]: 18 cases exhibited *ATM* promoter methylation as determined by MSP analysis, 15/23[3]: 15 cases exhibited ≤3-fold reduction of *ATM* mRNA levels compared to human mammary epithelial cell line, HMEC (all of the 15 cases exhibited aberrant methylation of the *ATM* promoter region); D (n=99)[4]: 75% of the tumours analyzed exhibited reduced levels of ATM compared to normal specimens assessed by IHC; 1/25[5]: all 25 cases had lost the other allele (LOH); 1/9[6]: the authors found that *ATM* is disrupted in one case by fluorescence *in situ* hybridization; 2/7[7]: 2 cases exhibited allelic loss of ATM (the authors did not find any mutation in the remaining allele of these two cases with LOH); D:7/17[7]: ATM nuclear staining was absent or low in the cancer cells of 7 cases compared to their normal counterparts; 3 patients had received chemotherapy/hormonotherapy before study; 18/59[8]: 18 cases exhibited low or absent levels of ATM as examined with IHC (compared to non-neoplastic tissue); E[9]: the authors found no mutations in *ATM* (the number of cases examined is not mentioned); D(n=39)[9]: the mRNA levels of *ATM* were low in the breast carcinomas and intermediate in the benign lesions compared to the normal breast tissue (F-test, p=0.0013); 7/16[10]: LOH of the *ATM* region occurred with the same frequency in advanced and in early stages; I(32/49)[11], N(12/49)[11], D(5/49)[11]: 32 cases exhibited higher levels of ATM immunostaining in the cancerous region versus normal specimens, 12 cases exhibited similar levels of ATM immunostaining between the cancerous areas and the normal counterparts, 5 cases exhibited low or no detectable levels of ATM immunostaining in the cancerous areas versus the normal specimens; 2/30[12]: the authors found, apart from the 2 already mentioned cases, an

additional specimen with a mutation within the 3'-UTR region of *ATM*; I: 10/32[13], N: 12/32[13], D: 10/32[13]: in all cases ATM protein levels were examined with IHC; 25/100[14]: 25 cases exhibited *ATM* promoter methylation as assessed by MSP analysis; in the same study, analysis of 8 non-cancerous tonsillectomy tissues indicated no methylation in the promoter region of *ATM*; No significant difference (n=24)[15]: no significant difference in the methylation status of the *ATM* promoter were observed between the tumour versus the normal counterpart (assessed by pyrosequencing analysis, n=24 samples); 31/53[15], 22/53[15]: ATM status was examined with WB, 59/135[15]: ATM status was assessed with immunohistochemistry, 49/105[16]: 49 cases exhibited *ATM* promoter methylation as examined by MSP analysis. In the same study in a subset of the 105 cases (n=31), the authors examined in paired tumour and surrounding normal counterparts the methylation status of *ATM* promoter region and found that the average methylation status of *ATM* promoter region was 69% in tumour versus 59% in normal counterparts; 16/32[17]: 16 cases exhibited *ATM* promoter methylation as assessed by MSP analysis. In the same study none of the 27 control samples (DNA extracted from non-malignant thyroid tissue) examined, exhibited *ATM* promoter methylation; D:18/18[18]: in 17 cases ATM immunostaining was absent and in one case ATM immunostaining was weak in Hodgkin Reed-Sternberg cells compared to the strong ATM immunostaining of the surrounding reactive cells in each case; ½[19]: 1 case with LOH in *ATM* locus exhibited a mutation in the remaining allele; 2/8[19]: 1 case exhibited no ATM immunostaining and the other case weak ATM immunostaining in Hodgkin Reed-Sternberg cells, with the remaining cases exhibiting strong ATM immunostaining of Hodgkin Reed-Sternberg cells (in all specimens small lymphocytes exhibited strong ATM immunostaining and served as internal control); 10/74[20]: 10 cases exhibited loss at the 11q14-q23 locus; examination of 5 cases with loss at the 11q14-q23 region revealed that 4/5 cases exhibited loss of *ATM*; 6/49[21]: 6 cases exhibited *ATM* promoter hypermethylation; 0/25[22], 0/49[22]: the authors found no evidence of hypermethylation of the *ATM* promoter, as assessed by MSP; 13/38[23]: 13 cases (12 cases with mantle cell lymphoma and 1 case with peripheral T cell lymphoma) exhibited according to the author's study deleterious mutations (refer to sequence alterations that adversely affect ATM function), 8/17[24]: 5 cases exhibited complete absence of ATM protein status and 3 cases showed low levels of ATM protein levels compared to normal tonsils; 5/5[25]: 5 cases exhibited both a mutation in one *ATM* allele and loss of the remaining one, 0/45[25]: none of the cases examined exhibited promoter hypermethylation, assessed by MSP; 0/17[26]: none of the 17 cases with follicle center lymphoma exhibited mutations in *ATM*; 9/12[27]: 7/9 cases with mutated *ATM* exhibited loss of the remaining allele (LOH), while in the remaining 2 cases both *ATM* alleles were mutated; 29/81[28]: 37/81 cases exhibited loss of 11q, further narrowing the minimal area of 11q loss resulted in the identification of 29/37 cases exhibiting loss of *ATM*; 2/2[29]: in both cases with a mutation in *ATM* gene, the remaining allele was lost (<10% of the presence of the wild type of ATM allele in tumour DNA); 15/17[29]: in 15 cases with mutated *ATM* the remaining allele was lost (<40% of the presence of the wild type of ATM allele in tumour DNA); 10/36[30]: 8 cases exhibited LOH and 2 cases had homozygous deletion for *ATM*; 4/15[29]: all 4 cases with decreased ATM protein levels had aberrations in *ATM* (2 with LOH and 2 with homozygous deletion);

41/399[31]: untreated cases, 14/83[31]: cases studied after cytotoxic therapy; 18/155[32]: in 4 cases one *ATM* allele was lost and the remaining one was mutated, in 3 cases both *ATM* alleles were mutated; 9/155[32]: in 9 cases there was a deletion in 11q locus; 7/27[33]: 5 cases with mutated *ATM* exhibited loss of the other allele, while the remaining 2 cases with mutated *ATM* are examined from a panel of 5 cases did not exhibit deletion at the *ATM* locus; D:34% (n=111)[34]: in all cases ATM protein levels were examined with Radioimmunoassay (RIA), cases with ATM levels <0.2 as compared to normal ones were verified with WB analysis (n=111, total number of cases examined); 5/8[35], 3/8[35]: 2 cases had been treated with alemtuzumab prior to enrolling in the study; 6/6[36]: all 6 cases with mutated *ATM* had lost the remaining allele; 25%(n=8)[37]: 25% of informative cases exhibited LOH in 11q region (n= number of cases examined); CGARN[65]: The Cancer Genome Atlas Research Network; 0/72[38]: untreated cases, 1/19[38]: cases studied after treatment with chemotherapy.

References related to Supplementary Table 3

1. Bozhanov, S. S. *et al.* Alterations in p53, BRCA1, ATM, PIK3CA, and HER2 genes and their effect in modifying clinicopathological characteristics and overall survival of Bulgarian patients with breast cancer. *J. Cancer Res.Clin. Oncol.* **136**, 1657-1669 (2010).
2. Treilleux, I. *et al.* The molecular causes of low ATM protein expression in breast carcinoma; promoter methylation and levels of the catalytic subunit of DNA-dependent protein kinase. *Histopathology* **51**, 63-69 (2007).
3. Ye, C. *et al.* Expression patterns of the ATM gene in mammary tissues and their associations with breast cancer survival. *Cancer* **109**, 1729-1735 (2007).
4. Vo, Q. N. *et al.* The ATM gene is a target for epigenetic silencing in locally advanced breast cancer. *Oncogene* **23**, 9432-9437 (2004).
5. Angèle, S., Treilleux, I., Brémond, A., Tanière, P. & Hall, J. Altered expression of DNA double-strand break detection and repair proteins in breast carcinomas. *Histopathology* **43**, 347-353 (2003).
6. Rodriguez, C. *et al.* Involvement of ATM missense variants and mutations in a series of unselected breast cancer cases. *Gen. Chrom. Cancer* **33***,* 141-149 (2002).
7. Lu, Y. *et al.* Disruption of the ATM gene in breast cancer. *Cancer Genet. Cytogenet* **126***,* 97-101 (2001).
8. Angèle, S. *et al.* Abnormal expression of the ATM and TP53 genes in sporadic breast carcinomas. *Clin. Cancer Res*. **6**, 3536-3544 (2000).
9. Kovalev, S., Mateen, A., Zaika, A. I., O' Hea, B. J., & Moll, U. M. Lack of defective expression of the ATM gene in sporadic breast cancer tissues and cell lines. *Int. J. Oncol*. **16***,* 825-831 (2000).
10. Kairouz, R. *et al.* ATM protein synthesis patterns in sporadic breast cancer. *Mol. Pathol.* **52***,* 252-256 (1999).
11. Rio, P. G. *et al.* Loss of heterozygosity of BRCA1, BRCA2 and ATM genes in sporadic invasive ductal breast carcinoma. *Int. J. Oncol.* **13***,* 849-853 (1998).
12. Waha, A. *et al.* Expression of the ATM gene is significantly reduced in sporadic breast carcinomas. *Int. J. Cancer* **78***,* 306-309 (1998).
13. Vorechovský, I. *et al.* The ATM gene and susceptibility to breast cancer: analysis of 38 breast tumors reveals no evidence for mutation. *Cancer Res.* ***56****,* 2726-2732 (1996).
14. Koike, M. *et al.* Ovarian cancer: loss of heterozygosity frequently occurs in the ATM gene, but structural alterations do not occur in this gene. *Oncology* **56**, 160-163 (1999).
15. Angèle, S. *et al.* ATM protein overexpression in prostate tumors: possible role in telomere maintenance. *Am. J. Clin. Pathol.* **121**, 231-236 (2004).
16. Milne, A. N. *et al.* Molecular analysis of primary gastric cancer, corresponding xenografts, and 2 novel gastric carcinoma cell lines reveals novel alterations in gastric carcinogenesis. *Hum. Pathol.* **38**, 903-913 (2007).
17. Zhang, L. *et al.* Alteration of the ATM gene occurs in gastric cancer cell lines and primary tumors associated with cellular response to DNA damage. *Mutat. Res.* **557***,* 41-51 (2004).

18. He, Y., Chen, Q. & Li, B. ATM in oral carcinogenesis: association with clinicopathological features. *J. Cancer. Res. Clin. Oncol.* **134**, 1013-1020 (2008).
19. Ai, L. *et al.* Ataxia-telangiectasia-mutated (ATM) gene in head and neck squamous cell carcinoma: promoter hypermethylation with clinical correlation in 100 cases. *Cancer Epidemiol. Biomarkers Prev.* **13,** 150-156 (2004).
20. Safar, A. M. *et al.* Methylation profiling of archived non-small cell lung cancer: a promising prognostic system. *Clin. Cancer Res.* **11***,* 4400-4405 (2005).
21. Smith, J. A., Fan, C. Y., Zou, C., Bodenner, D. & Kokoska, M. S. Methylation status of genes in papillary thyroid carcinoma. *Arch. Otolaryngol. Head Neck Surg.* **133***,* 1006-1011 (2007).
22. Bose, S. *et al.* Down-regulation of ATM protein in HRS cells of nodular sclerosis Hodgkin's lymphoma in children occurs in the absence of ATM gene inactivation. *J. Pathol.* **213,** 329-336 (2007).
23. Lespinet, V. *et al.* Single-cell analysis of loss of heterozygosity at the ATM gene locus in Hodgkin and Reed-Sternberg cells of Hodgkin's lymphoma: ATM loss of heterozygosity is a rare event. *Int. J. Cancer* **114***,* 909-916 (2005).
24. Liberzon, E. *et al.* Molecular variants of the ATM gene in Hodgkin's disease in children. *Br. J. Cancer* **90**, 522-525 (2004).
25. Kawamata, N. *et al*. Identified hidden genomic changes in mantle cell lymphoma using high-resolution single nucleotide polymorphism genomic array. *Exp. Hematol.* **37***,* 937-946 (2009).
26. Jardin, F. *et al*. Detection of gene copy number aberrations in mantle cell lymphoma by a single quantitative multiplex PCR assay: clinicopathological relevance and prognosis value. *Br. J. Haematol.* **146***,* 607-618 (2009).
27. Gumy-Pause, F. *et al*. Detection of ATM gene deletion/duplication by multiplex ligation-dependant probe amplification in childhood lymphoid malignancies: a report from the Children's Oncology Group. *Leuk. Res.* **32,** 1207-1213 (2008).
28. Salaverria, I. *et al*. Genomic profiling reveals different genetic aberrations in systemic ALK-positive and ALK-negative anaplastic large cell lymphomas. *Br. J. Haematol.* **140***,* 516-526 (2008).
29. Huang, Q. *et al*. Promoter hypermethylation of multiple genes in gastric lymphoma. *Leuk. Lymphoma* **48***,* 1988-1996 (2007).
30. Gumy-Pause, F., Wacker, P., Maillet, P., Betts, D. R. & Sappino, A. P. ATM alterations in childhood non-Hodgkin lymphoma. *Cancer Genet. Cytogenet*. **166***,* 101-111 (2006).
31. Gumy-Pause, F., Wacker, P., Maillet, P., Betts, D. R. & Sappino, A. P. ATM promoter analysis in childhood lymphoid malignancies: a brief communication. *Leuk. Res.* **30**, 335-337 (2006).
32. Fang, N. Y. *et al.* Oligonucleotide microarrays demonstrate the highest frequency of ATM mutations in the mantle cell subtype of lymphoma. *Proc Natl Acad Sci USA* **100**, 5372-5377 (2003).
33. Camacho, E. *et al.* ATM gene inactivation in mantle cell lymphoma mainly occurs by truncating mutations and missense mutations involving the phosphatidylinositol-3 kinase domain and is associated with increasing numbers of chromosomal imbalances. *Blood* **99,** 238-244 (2002).

34. Grønbaek, K. *et al.* ATM mutations are associated with inactivation of the ARF-TP53 tumor suppressor pathway in diffuse large B-cell lymphoma. *Blood* **100,** 1430-1437 (2002).
35. Lossos, I. S. *et al.* Mutation of the ATM gene is not involved in the pathogenesis of either follicle center lymphoma or its transformation to higher-grade lymphoma. *Leuk. Lymphoma* **43**, 1079-1085 (2002).
36. Cuneo, A. *et al.* Acquired chromosome 11q deletion involving the ataxia teleangiectasia locus in B-cell non-Hodgkin's lymphoma: correlation with clinicobiologic features. *J. Clin. Oncol*. **18***,* 2607-2614 (2000).
37. Schaffner, C., Idler, I., Stilgenbauer, S., Döhner, H. & Lichter, P. Mantle cell lymphoma is characterized by inactivation of the ATM gene. *Proc. Natl. Acad. Sci. USA* **97***,* 2773-2778 (2000).
38. Stilgenbauer, S. *et al.* Molecular characterization of 11q deletions points to a pathogenic role of the ATM gene in mantle cell lymphoma. *Blood* **94**, 3262-3264 (1999).
39. Vorechovský, I. *et al.* Clustering of missense mutations in the ataxia-telangiectasia gene in a sporadic T-cell leukaemia. *Nat. Genet.* **17**, 96-99 (1997).
40. Gumy-Pause, F., Wacker, P., Maillet, P., Betts, D. R. & Sappino, A. P. ATM variants and predisposition to childhood T-lineage acute lymphoblastic leukaemia. *Leukemia* **20**, 526-527 (2006).
41. Gumy Pause, F., Wacker, P., Maillet, P., Betts, D. R. & Sappino, A. P. ATM gene alterations in childhood acute lymphoblastic leukemias. *Hum. Mutat*. **21**, 554 (2003).
42. Haidar, M. A. *et al.* ATM gene deletion in patients with adult acute lymphoblastic leukemia. *Cancer* **88***,* 1057-1062 (2000).
43. Takeuchi, S. *et al.* Identification of three distinct regions of deletion on the long arm of chromosome 11 in childhood acute lymphoblastic leukemia. *Oncogene* **18***,* 7387-7388 (1999).
44. Takeuchi, S. *et al.* The ATM gene and susceptibility to childhood T-cell acute lymphoblastic leukaemia*. Br. J. Haematol.* **103***,* 536-538 (1998).
45. Haferlach, C. *et al.* Toward a comprehensive prognostic scoring system in chronic lymphocytic leukemia based on a combination of genetic parameters. *Genes Chromosomes Cancer* **49,** 851-859 (2010).
46. Leuenberger, M. *et al.* AID protein expression in chronic lymphocytic leukemia/small lymphocytic lymphoma is associated with poor prognosis and complex genetic alterations. *Mod. Pathol*. **23***,* 177-186 (2010).
47. Xu, W. *et al.* Prognostic significance of ATM and TP53 deletions in Chinese patients with chronic lymphocytic leukemia. *Leuk. Res.* **32***,* 1071-1077 (2008).
48. Austen, B. *et al.* Mutations in the ATM gene lead to impaired overall and treatment-free survival that is independent of IGVH mutation status in patients with B-CLL. *Blood* **106***,* 3175-3182 (2005).
49. Eclache, V. *et al.* Cryptic deletion involving the ATM locus at 11q22.3 approximately q23.1 in B-cell chronic lymphocytic leukemia and related disorders. *Cancer Genet. Cytogenet*. **152***,* 72-76 (2004).
50. Schaffner, C., Stilgenbauer, S., Rappold, G. A., Döhner, H. & Lichter, P. Somatic ATM mutations indicate a pathogenic role of ATM in B-cell chronic lymphocytic leukemia. *Blood* **94,** 748-753 (1999).

51. Stankovic, T. *et al.* Inactivation of ataxia telangiectasia mutated gene in B-cell chronic lymphocytic leukaemia. *Lancet* **353**, 26-29 (1999).
52. Bullrich, F. *et al.* ATM mutations in B-cell chronic lymphocytic leukemia. *Cancer Res.* **59***,* 24-27 (1999).
53. Starostik, P. *et al.* Deficiency of the ATM protein expression defines an aggressive subgroup of B-cell chronic lymphocytic leukemia*. Cancer Res.* **58***,* 4552-4557 (1998).
54. Stoppa-Lyonnet, D. *et al.* Inactivation of the ATM gene in T-cell prolymphocytic leukemias. *Blood* **91,** 3920-3926 (1998).
55. Yuille, M. A. *et al.* ATM is usually rearranged in T-cell prolymphocytic leukaemia. *Oncogene* **16***,* 789-796 (1998).
56. Stilgenbauer, S. *et al.* Biallelic mutations in the ATM gene in T-prolymphocytic leukemia. *Nat. Med.* **3***,* 1155-1159 (1997).
57. Stilgenbauer, S. *et al.* Molecular cytogenetic delineation of a novel critical genomic region in chromosome bands 11q22.3-923.1 in lymphoproliferative disorders. *Proc. Natl. Acad. Sci. USA* **93**, 11837-11841 (1996).
58. Liberzon, E. *et al.* ATM gene mutations are not involved in medulloblastoma in children. *Cancer Genet. Cytogenet*. **146**, 167-169 (2003).
59. Greenman, C. *et al.* Patterns of somatic mutation in human cancer genomes. *Nature* **446,** 153-158 (2007).
60. Wood, L. D. *et al.* The genomic landscapes of human breast and colorectal cancers. *Science* **318,** 1108-1113 (2007).
61. Corbo, V. *et al.* Mutational profiling of kinases in human tumours of pancreatic origin identifies candidate cancer genes in ductal and ampulla of vater carcinomas. *PLoS One* **5***,* e12653 (2010).
62. Jones, S. *et al.* Core signaling pathways in human pancreatic cancers revealed by global genomic analyses. *Science* **321**, 1801-1806 (2008).
63. Ding, L. *et al.* Somatic mutations affect key pathways in lung adenocarcinoma. *Nature* **455**, 1069-1075 (2008).
64. Parsons, D. W. *et al.* An integrated genomic analysis of human glioblastoma multiforme. *Science* **321**, 1807-1812 (2008).
65. Cancer Genome Atlas Research Network. Comprehensive genomic characterization defines human glioblastoma genes and core pathways. *Nature* **455**, 1061-1068 (2008).